

Jump-starting relativistic flows, and the M87 jet

Maxim Lyutikov, Ahmad Ibrahim
Department of Physics and Astronomy, Purdue University,
525 Northwestern Avenue, West Lafayette, IN 47907-2036

Abstract

We point out the dominant importance of plasma injection effects for relativistic winds from pulsars and black holes. We demonstrate that outside the light cylinder the magnetically dominated outflows while sliding along the helical magnetic field move in fact nearly radially with very large Lorentz factors $\gamma_0 \gg 1$, imprinted into the flow during pair production within the gaps. Only at larger distances, $r \geq \gamma_0(c/\Omega)$, the MHD acceleration $\Gamma \propto r$ takes over. As a result, Blandford-Znajek (BZ) driven outflows would produce spine-brightened images. The best-resolved case of the jet in M87 shows both bright edge-brightened features, as well as weaker spine-brightened feature. Only the spine-brightened component can be BZ-driven/originate from the BH's magnetosphere.

1. Introduction

Acceleration of relativistic winds and jets is a classical problem in high energy astrophysics (*e.g.* Michel 1969; Goldreich & Julian 1970; Blandford & Znajek 1977; Blandford & Königl 1979; Camenzind 1986; Krolik 1999; McKinney 2006; Barkov & Komissarov 2008; Blandford et al. 2019). A standard approach involves solution of the MHD equation (analytical or numerical) starting with a slowly moving plasma. Plasma is then accelerated by the corresponding pressure gradient, and collimated by magnetic hoop stresses (Blandford & Payne 1982).

Observations of the inner part of the jet in M87, down to just 7 Schwarzschild radii, shows complicated structure. First, one observes limb-brightened collimated jet - the jet accelerating smoothly, with a parabolic profile Nakamura & Asada (2013); Kim et al. (2018); Blandford et al. (2019), Fig. 1.

In addition to limb-brightened structures, Lu et al. (2023) recently detected a new feature - spine-brightened jet.

In this work we aim to model the emission pattern expected in the Blandford & Znajek (1977) model of jet acceleration and compare with the observation. The key new ingredient in our work is taking into account large initial (injection) velocities parallel to the local magnetic field.

MHD models of acceleration (Beskin 2009; Komissarov et al. 2009; Nokhrina & Beskin 2017) take full account of plasma velocity: both along and across magnetic field. The corresponding analytical treatment, based on the relativistic Grad-Shafranov equation (Grad 1967; Shafranov

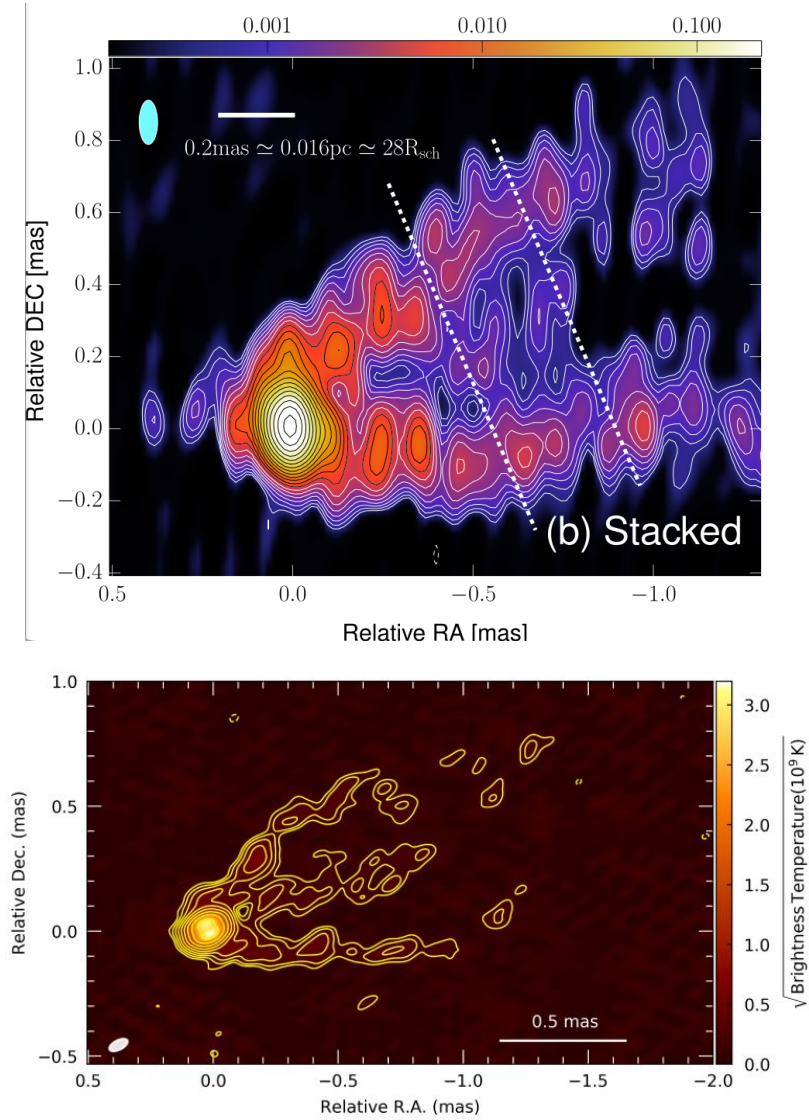


Fig. 1.— Top: Central part of jet in M87 at 86 GHz showing limb-brightened jet (Kim et al. 2018). Bottom: spine-brightened structure (Lu et al. 2023)

1966; Scharlemann & Wagoner 1973; Beskin 2009) is completed, as it requires finding the initially unknown current distribution together with the solution for the magnetic field.

In the limit of highly magnetized plasma - the force-free limit - the parallel velocity is not defined in principle. But that does not mean it can be neglected. Plasma may be/is streaming with large Lorentz factors along magnetic fields. It seems this particular aspect was/is not considered previously. But it is highly important as we argue here.

Models of gaps in black hole magnetospheres (Hirotani & Okamoto 1998; Blandford & Znajek 1977; Levinson 2000; Levinson & Rieger 2011; Ptitsyna & Neronov 2016) generally predict that magnetospheric gaps, with thickness much smaller than the size of the magnetosphere (the light cylinder) accelerate particles with Lorentz factors $\sim 10^3 - 10^4$; accelerated particles first IC scatter soft disk photons, this is followed by two-photon pair production, and the electromagnetic cascade. Resulting Lorentz factors are of similar values, $\sim 10^3 - 10^4$. Lorentz factors up to $\sim 10^6$ are also possible (Ptitsyna & Neronov 2016).

In MHD simulations, first, high magnetization is hard to achieve and, second, plasma is typically injected at rest (*e.g.* Tomimatsu 1994). In the corresponding PIC simulations particles are typically injected at rest (*e.g.* Chen & Beloborodov 2014; Philippov et al. 2015; Crinquand et al. 2020; Hakobyan et al. 2022).

Perhaps the closest approach to the current one is Beskin & Kuznetsova (2000), where the importance of injection for the structure of the magnetosphere and the corresponding energy relations were discussed, quote "it is the pair creation region that plays the role of the energy source" (Beskin et al. 1992, is also relevant).

2. The approach and the conclusion

We start with a force-free solution and add particle dynamics along the field kinematically, in the bead-on-wire approximation, neglecting its back reaction on the structure of the magnetic field. The bead-on-wire approach has a clear advantage: for a given structure of the magnetic field the particle dynamics is easily calculated in *algebraic form* (see also Section 7.2.6 of Gralla & Jacobson 2014). No integration of the equations of motion is needed and no special conditions (*e.g.* at Alfvén or fast surfaces) appear. The drawback is that it does not provide the full picture of what the magnetic field structure is: the structured the magnetosphere should be prescribed. Thus, our approach can be seen as the next term in expansion in magnetization parameter $1/\sigma \ll 1$: force-free solution in the limit $1/\sigma \rightarrow 0$ provide the structure of the magnetic field, the next term takes in the account particle dynamics in the prescribed magnetic field.

As a start, we assume that flow lines and magnetic flux surfaces are conical. (More complicated collimated flux surfaces behave similarly, see §5.1). In flat metrics, there is then analytical solution for the monopolar magnetic field due to Michel (1973) (it can be generalized to Schwarzschild case).

We use it as a starting point:

$$\begin{aligned}
 B_r &= \frac{r_0^2}{r^2} B_0 \\
 B_\phi &= -\frac{r_0^2 \sin \theta \Omega}{r} B_0 = E_\theta \\
 \vec{\beta}_{EM} &= \left\{ \frac{r^2 \sin^2 \theta \Omega^2}{1 + r^2 \sin^2 \theta \Omega^2}, 0, \frac{r \Omega \sin(\theta)}{1 + r^2 \sin^2 \theta \Omega^2} \right\} \\
 \Gamma_{EM} &= \sqrt{1 + r^2 \Omega^2 \sin^2(\theta)} \tag{1}
 \end{aligned}$$

This analytical force-free solution of the pulsar equation (Scharlemann & Wagoner 1973; Beskin 2009) passes smoothly through the light cylinder (Alfvén surface) $R_{LC} = c/(\sin \theta \Omega)$. Numerical models of the inner wind indicate that the structure of the electromagnetic fields quickly approaches Michel’s solution Prokofev et al. (2018). Komissarov (2004) showed that monopolar geometry of magnetic field lines is also a good approximation in case of a black hole in external magnetic field.

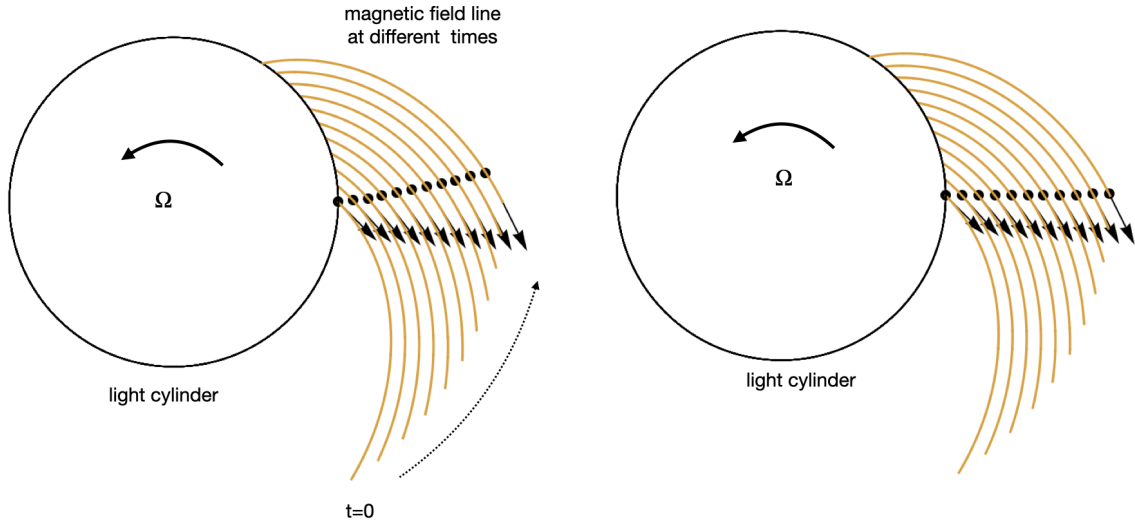


Fig. 2.— Particles’ trajectories calculated in Michel’s field outside the light cylinder for Lorentz factors $\gamma_0 = 2, 10$, Eq. (A7). The circle is the light cylinder, orange curves indicate the same magnetic field line at consecutive movements, arrows are directions of particle velocity at each point, and black dots are the location of the particle. These calculations illustrate that for $\gamma_0 \gg 1$ the trajectory is nearly radial.

As long as the force-free condition is satisfied (negligible inertial effects) arbitrary initial motion of (charge neutral) plasma can be added along the field. Conditions at the light cylinder remain

unchanged. The total velocity is then the (relativistic) sum of the electromagnetic velocity (1) and the motion along the rotating magnetic field.

It turns out that a particle launched with large Lorentz factor along the rotating magnetic spiral (in a bead-on-wire approximation) moves nearly radially, Fig. 2. This has been a known effect from numerical analysis (Contopoulos et al. 2020), and was recently analytically discussed by Lyutikov (2022). The key point is that the azimuthal motion along the spiral is nearly compensated by the motion of the spiral itself. In this paper we generalize the results of Lyutikov (2022) for particle dynamics in rotating winds to the curved space of Schwarzschild and Kerr black holes.

The observed emission pattern from relativistically moving particles is dominated by the Doppler factor δ . For axisymmetric jet the largest Doppler factor is along the flow lines that project to the spine of the image, Fig. 3.

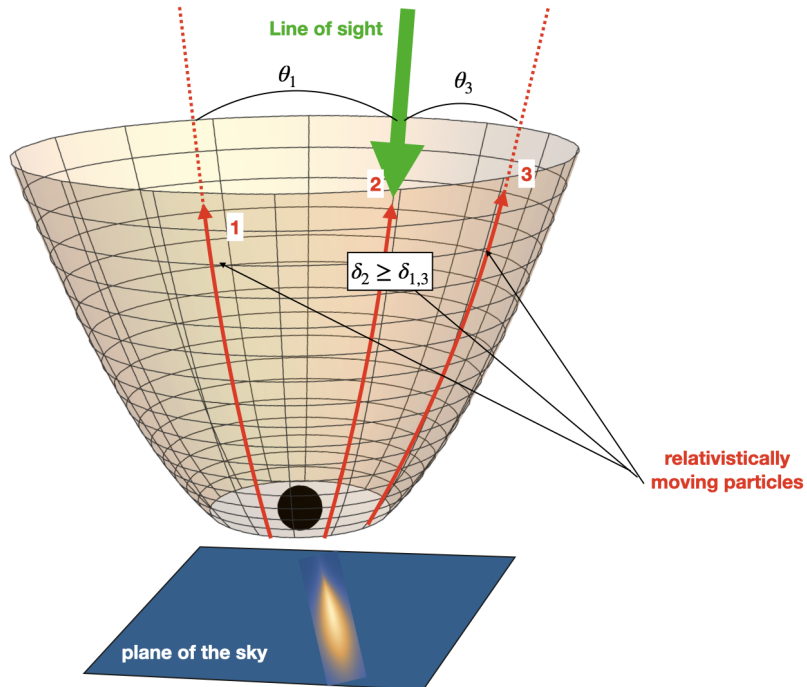


Fig. 3.— Graphic explanation why BZ-produced jets are expected to be spine-brightened. Shown are flux surfaces and three different particles’ trajectories. Emission produced by particle 2 has the smallest angle with respect to the line of sight, largest Doppler factor, and would result in brightest emission pattern.

Thus, relativistic flows emanating from within the magnetosphere, driven by the BZ process, are expected to produce spine-brightened image. This is consistent with observations of a weak central spine in M87 jet, Fig. 1 bottom panel. On the other hand, the edge-brightened emission observed by Kim et al. (2018) is inconsistent with the BZ process. The edge-brightened part is

not centered on the black hole. This implies that a flow is only mildly relativistic. For example, estimates of the viewing angle $15^\circ - 30^\circ$ degrees (Bicknell & Begelman 1996) imply bulk Lorentz factors $\sim 3 - 2$ (otherwise the emission would have been beamed away).

We then conclude that the limb-brightened and spine-brightened parts of the M87 jet have different origin: the spine-brightened part originates within the BH magnetosphere driven by the Blandford-Znajek mechanism (Blandford & Znajek 1977). The edge-brightened component should have a different origin. For example, it can be produced by the Blandford & Payne (1982) mechanism, starting as a slow accelerating flow from the accretion disk.

3. Particle motion along rotating spiral

3.1. General relations

The motion of a particle in bead-on-wire approximation can be derived algebraically for a given structure of magnetosphere in the case of flat, Schwarzschild and Kerr metrics. As a basic case, we start with particles moving in the equatorial plane in case of Kerr metric. We start with a particular case of Archimedian spiral with radial step equal $1/\Omega$.

We use the machinery of General Relativity to treat particle motion in the rotating frame, in curved space-time. We start at the equatorial plane $\theta = \pi/2$ of Kerr metric. For flat and Schwarzschild cases, where monopolar magnetic field is an exact solution, the generalization to motion with fixed arbitrary polar angle is recovered later.

The results of this section are further re-derived/extended in the Appendices. In Appendix A we re-derive the corresponding relations using Lagrangian and Hamiltonian approaches for relativistic particle moving along a constrained path in flat space-time. In Appendix B we use alternative formulation of the Lagrangian. In section 3.5 we allow for arbitrary radial step (effective, taking into account non-force-free effects of plasma loading). Finally, in the most mathematically advanced approach, in Appendix D we discuss the most general case of field structure in Kerr metric.

Kerr metric in the equatorial plane is defined by the metric tensor

$$\begin{aligned}
 g_{00} &= 1 - \frac{2M}{r} = \alpha^2 \\
 g_{rr} &= \frac{r^2}{\Delta} \\
 g_{\phi\phi} &= a^2 M^2 + r^2 + \frac{2a^2 M^3}{r} \equiv \Delta_1 \\
 g_{0\phi} &= -\frac{2aM^2}{r} \\
 \Delta &= a^2 M^2 - 2Mr + r^2 \\
 \Delta_1 &= a^2 M^2 + r^2 + \frac{2a^2 M^3}{r}
 \end{aligned} \tag{2}$$

where a is the dimensionless Kerr parameter.

Consider rotating black hole magnetosphere. Since we use bead-on-wire approximation, we first need to find a structure of a given magnetic field line. The rotating spiral is defined by two parameters: the angular velocity of rotation Ω and radial step c/Ω_1 . In the force-free approximation, $\Omega = \Omega_1$ (see Appendix 3.5 for a generalization $\Omega_1 \neq \Omega$), the fast electromagnetic mode propagates radially with (setting $ds = 0$ for null trajectory and $d\phi = 0$ for radial propagation)

$$\beta_F = \sqrt{\frac{\Delta(r - 2M)}{r^3}} = \frac{\alpha\sqrt{\Delta}}{r} \rightarrow \alpha^2 \tag{3}$$

(the latter limit is for Schwarzschild case).

Angular velocity of the Lense-Thirring precession

$$\omega_{LT} = a \frac{2M^2}{r^3 + a^2 M^2 (2M + r)} = \frac{2aM^2}{r\Delta_1} = -\frac{g_{0\phi}}{g_{\phi\phi}} \tag{4}$$

Thus, the radial step of the spiral is given by

$$\begin{aligned}
 d\phi' &= \omega_{sp} dr \\
 \omega_{sp} &= \frac{\omega_{LT} - \Omega}{\beta_F} = -\sqrt{\frac{g_{rr}}{g_{00}}} \left(\frac{g_{0\phi}}{g_{\phi\phi}} + \Omega \right)
 \end{aligned} \tag{5}$$

(For propagation with sub-luminal velocity, see Appendix 3.5. In this case the radial step is smaller than $1/\Omega$. This can be due to back-reaction of plasma on magnetic field lines.)

Next, in the Kerr metric, transferring to the frame rotating with the magnetic field (see Appendix C for corresponding limitations)

$$d\phi \rightarrow d\phi' + \Omega dt \tag{6}$$

and imposing the spiral constraint (5), we find metric coefficients in the rotating frame

$$\begin{aligned}
 G_{00} &= g_{00} - \left(g_{\phi\phi} \Omega - \frac{4aM^2}{r} \right) \Omega \\
 G_{rr} &= \frac{r^2}{\Delta} + g_{\phi\phi} \omega_{sp}^2 \\
 G_{0r} &= \left(-\frac{2aM^2}{r} + \Omega g_{\phi\phi} \right) \omega_{sp}
 \end{aligned} \tag{7}$$

The contra-variant metric is

$$\begin{aligned}
 G^{00} &= -\frac{G_{rr}}{\Delta_G} \\
 G^{rr} &= \frac{G_{00}}{\Delta_G} \\
 G^{0r} &= \frac{G_{0r}}{\Delta_G} \\
 \Delta_G &= G_{0r}^2 + G_{00}G_{rr}
 \end{aligned} \tag{8}$$

Using the Hamilton-Jacobi equation

$$G^{00}(\partial_t S)^2 + 2G^{0r}(\partial_t S)(\partial_r S) + G^{rr}(\partial_r S)^2 = 1 \tag{9}$$

with a separation

$$S = -\gamma_0 t + S_1(r), \tag{10}$$

we find

$$G^{00}\gamma_0^2 - 2G^{0r}\gamma_0(\partial_r S) + G^{rr}(\partial_r S)^2 = 1 \tag{11}$$

Thus,

$$(\partial_r S) = \frac{G_{0r}}{G_{00}} \gamma_0 \pm \frac{\sqrt{\Delta_G(\gamma_0^2 - G_{00})}}{G_{00}} \tag{12}$$

This equation can be analytically integrated in flat space, giving the trajectory $r(t)$ (Lyutikov 2022); see also alternative derivation in Appendix A, Eq. (A7). But deriving $r(t)$ is an unnecessary yet complicated step, since we are not interested in the time dependence of the particle velocity, only in its coordinate dependence.

Differentiating with respect to γ_0

$$\partial_{\gamma_0}(\partial_r S) = \frac{G_{0r}}{G_{00}} \pm \frac{\gamma_0}{G_{00}} \sqrt{\frac{\Delta_G}{\gamma_0^2 - G_{00}}} \tag{13}$$

Finally,

$$\beta_r = (\partial_{\gamma_0}(\partial_r S))^{-1} = \frac{G_{00}}{\gamma_0 \sqrt{(G_{00}G_{rr} + G_{0r}^2)/(\gamma_0^2 - G_{00})} + G_{0r}} \tag{14}$$

In equation (14), we ignored the negative solution because it represents going in a not interesting direction. We explain this more while re-deriving equation (14) by various Lagrangian approaches in Appendices A and B. This solves the problem of particle dynamics in rotating magnetosphere in the bead-on-wire approximation.

One of the mathematical complications involves changing the sign of G_{00} while crossing the light cylinder. However, the speed β_r stays positive. Explicit forms are given below, *e.g.* Eq. (17), passes smoothly through the light cylinder.

We point out that the Hamilton-Jacobi approach allows one to find trajectory purely algebraically - no integration of the equation of motion is involved.

Next, we give explicit relations for particular examples of flat, Schwarzschild, and Kerr spaces.

3.2. Flat space $M = 0$

In the frame rotating with the spiral the metric tensor is (See also Lyutikov 2022)

$$\begin{aligned} G_{00} &= 1 - \sin^2 \theta r^2 \Omega^2 \\ G_{0r} &= -\sin^2 \theta r^2 \Omega^2 \\ G_{rr} &= 1 + \sin^2 \theta r^2 \Omega^2 \end{aligned} \tag{15}$$

Gives Christoffel coefficients

$$\begin{aligned} \Gamma_{00}^0 &= r^3 \sin^4 \theta \Omega^4 \\ \Gamma_{0r}^0 &= -r \sin^2 \theta \Omega^2 (1 + \sin^2 \theta r^2 \Omega^2) \\ \Gamma_{rr}^0 &= r \sin^2 \theta \Omega^2 (2 + \sin^2 \theta r^2 \Omega^2) \\ \Gamma_{rr}^r &= r \sin^2 \theta \Omega^2 (1 + \sin^2 \theta r^2 \Omega^2) \\ \Gamma_{0r}^r &= -r^3 \sin^4 \theta \Omega^4 \\ \Gamma_{00}^r &= -r \sin^2 \theta \Omega^2 (1 - \sin^2 \theta r^2 \Omega^2) \end{aligned} \tag{16}$$

$$\beta_r = \frac{1 - \sin^2 \theta r^2 \Omega^2}{\frac{\gamma_0}{\sqrt{\gamma_0^2 + \sin^2 \theta r^2 \Omega^2 - 1}} - \sin^2 \theta r^2 \Omega^2} = \begin{cases} 1 - \frac{1}{2\gamma_0^2}, & \gamma_0 \gg r\Omega \sin \theta \\ 1 - \frac{1}{\sin^2 \theta r^2 \Omega^2} + \frac{\gamma_0}{\sin^3 \theta r^3 \Omega^3}, & r \rightarrow \infty \\ \frac{2\gamma_0^2}{1+2\gamma_0^2} \approx 1 - \frac{1}{2\gamma_0^2}, & r = 1/\Omega \end{cases} \tag{17}$$

The corresponding Lorentz factor $\gamma = 1/\sqrt{1 - \beta_r^2 - (\sin \theta r \Omega (1 - \beta_r))^2}$ is

$$\gamma = \frac{\gamma_0 - \sin^2 \theta r^2 \Omega^2 \sqrt{\gamma_0^2 + \sin^2 \theta r^2 \Omega^2 - 1}}{1 - \sin^2 \theta r^2 \Omega^2} = \begin{cases} \gamma_0 + \frac{\sin^2 \theta r^2 \Omega^2}{2\gamma_0}, & \gamma_0 \gg r\Omega \sin \theta \\ \sin \theta r \Omega + \frac{1+\gamma_0^2}{2r \sin \theta \Omega}, & r \rightarrow \infty \\ \gamma_0 + \frac{1}{2\gamma_0} + \frac{\sin \theta \Omega}{\gamma_0} \left(r - \frac{1}{\sin \theta \Omega} \right), & r \rightarrow 1/(\sin \theta \Omega) \end{cases} \tag{18}$$

see Fig. 4.

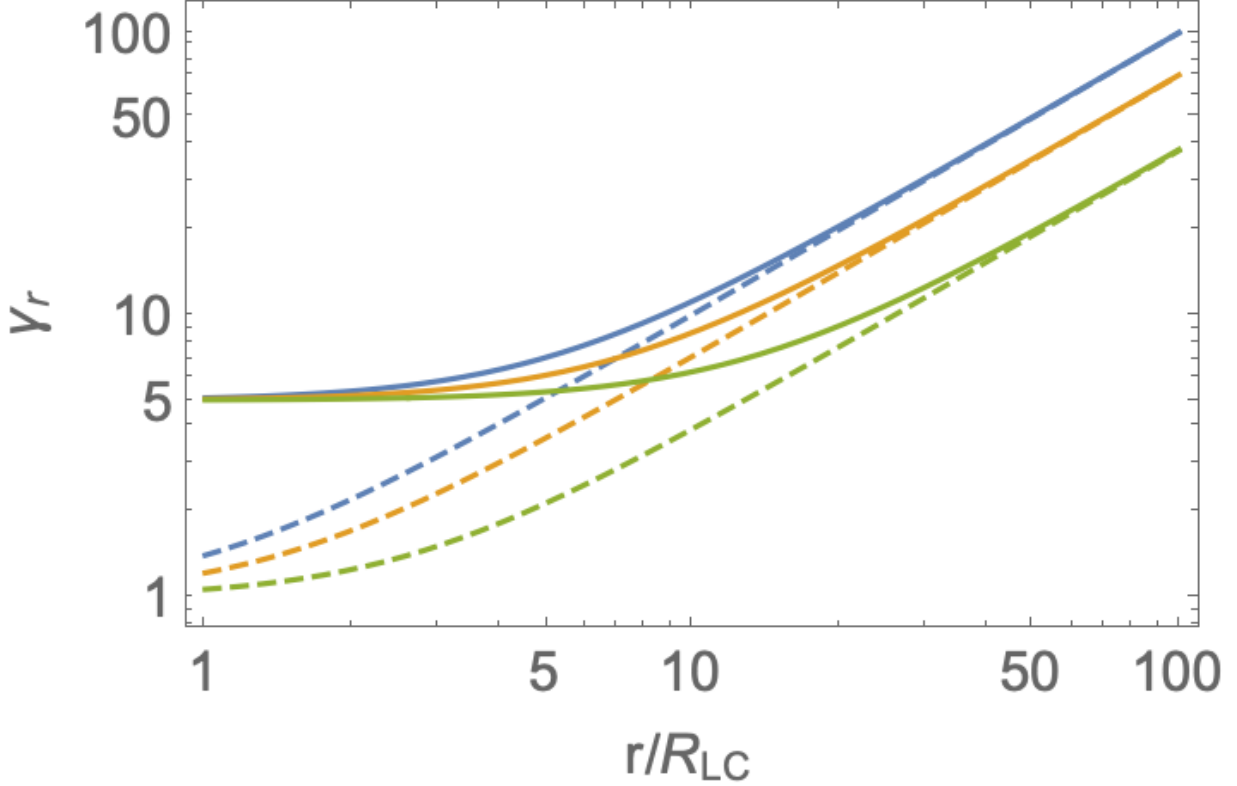


Fig. 4.— Lorentz factors corresponding to (18) compared with Michels’ solution $\gamma = \sqrt{1 + r^2\Omega^2 \sin^2 \theta}$ for $\gamma_0 = 5$ and $\theta = \pi/8, \pi/4, \pi/2$ (bottom to top). Only at large distances $r \geq \gamma_0 R_{LC}$ MHD acceleration picks up.

It may be verified using Lorentz transformations that the electric field in the frame of the particle is zero.

The integration constant γ_0 physically corresponds to some value of the energy at some location. With a change of parameter γ_0 , so that $\gamma_0 + 1/(2\gamma_0) \rightarrow \gamma_{LC}$, the solution would correspond to initial condition γ_{LC} on the light cylinder:

$$\beta_r = \frac{1 - \sin^2 \theta r^2 \Omega^2}{\frac{\gamma_{LC} + \sqrt{\gamma_{LC}^2 - 2}}{2\sqrt{\frac{1}{4}(\gamma_{LC} + \sqrt{\gamma_{LC}^2 - 2})^2 + \sin^2 \theta r^2 \Omega^2 - 1}} - \sin^2 \theta r^2 \Omega^2} \quad (19)$$

In what follows we skip this unnecessary redefinition. Numerically γ_0 is typically very close to the energy of the particle crossing the outer light cylinder, see *e.g.* (17). Also, in appendix (D) we discuss the range of the allowed values for this constant of motion and we show that this constant behaves the same as the initial Lorentz factor of a particle at the outer light cylinder when $\gamma_0 \gg 1$;

hence, we give this constant the symbol γ_0 .

Importantly, toroidal component of the velocity always remains small

$$\beta_\phi = \sin\theta r\Omega(1 - \beta_r) = \frac{\gamma_0 - \sqrt{\gamma_0^2 + r^2\Omega^2 \sin^2(\theta) - 1}}{\gamma_0 - r^2\Omega^2 \sin^2(\theta)\sqrt{\gamma_0^2 + r^2\Omega^2 \sin^2(\theta) - 1}} r\Omega \sin(\theta) \quad (20)$$

its maximal value is reached at $r \approx 1.27\gamma_0/\Omega$ and equals

$$\beta_{\phi,max} \approx 0.3/\gamma_0 \quad (21)$$

The angle of motion with respect to the radial direction, $\tan\chi = \beta_\phi/\beta_r$ always remains small, Fig. 5

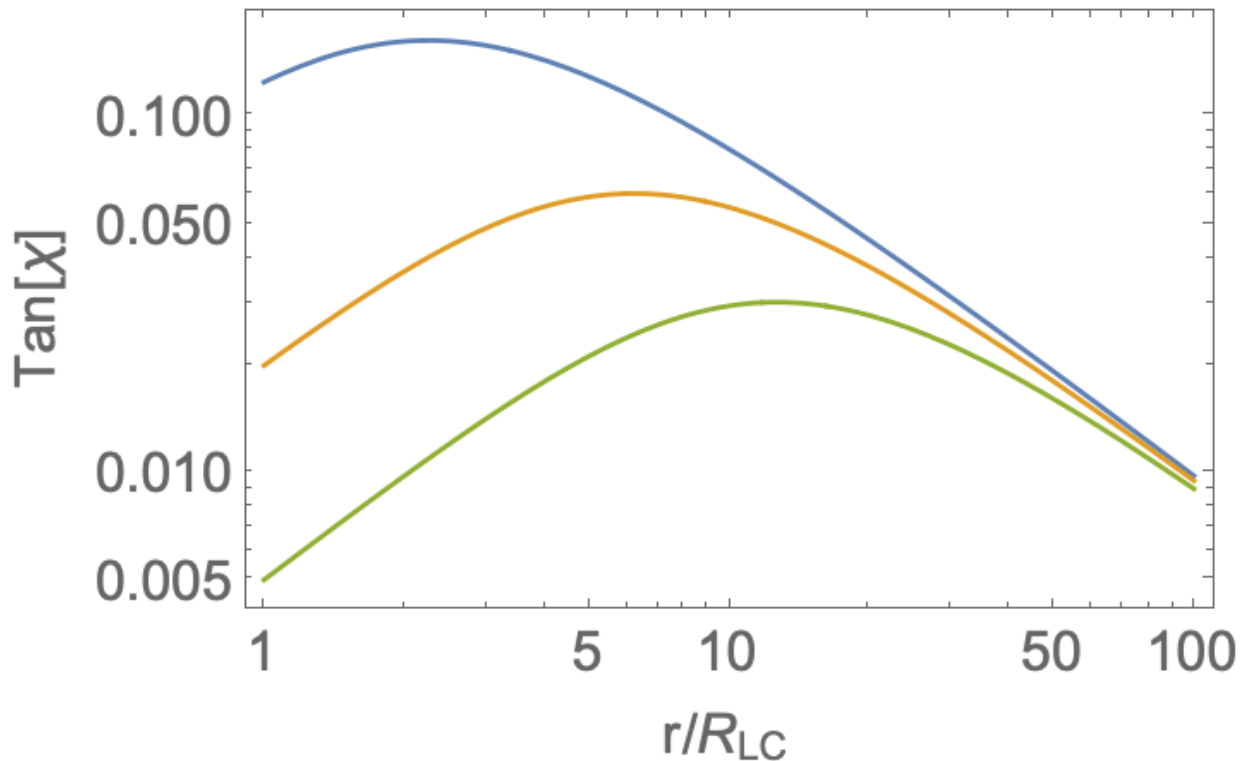


Fig. 5.— Angle of motion with respect to the radial direction, $\tan\chi = \beta_\phi/\beta_r$ for $\gamma_0 = 2, 5, 10$ (top to bottom); flat space $M = 0$. The motion is nearly radial.

We also note simple relations in terms of proper time τ (for $\theta = \pi/2$).

$$\begin{aligned} \frac{dr}{d\tau} &= \gamma \frac{dr}{dt} = \sqrt{\gamma_0^2 + r^2\Omega^2 - 1} \\ \frac{d^2r}{d\tau^2} &= r\Omega^2 \end{aligned} \quad (22)$$

Eq. (22) has a solution

$$\begin{aligned}\Omega r(\tau) &= \gamma_0 \sinh(\tau\Omega) + \cosh(\tau\Omega) \\ r'(\tau) &= \gamma_0 \cosh(\tau\Omega) + \sinh(\tau\Omega)\end{aligned}\tag{23}$$

(using $r(0) = 1/\Omega$ and $r'(0) = \gamma_0$). In proper time the Lorentz factor doubles approximately in $\tau \sim 1/\Omega$. This result is consistent with doubling in observer time in $t \sim \gamma_0/\Omega$, at distance $r \sim \gamma_0 R_{LC}$

3.3. Schwarzschild black hole, $a = 0$

Metric tensor is now

$$\begin{aligned}G_{00} &= \alpha^2 - \sin^2 \theta r^2 \Omega^2 = G^{rr} \\ G_{0r} &= -\sin^2 \theta \frac{r^2 \Omega^2}{\alpha^2} = G^{0r} \\ G_{rr} &= \alpha^{-2} + \sin^2 \theta \frac{r^2 \Omega^2}{\alpha^4} = G^{00} \\ ||G|| &= -1\end{aligned}\tag{24}$$

(a factor of minus one is explicitly included in the definition of the 0-0 component of the metric).

The Christoffel symbols evaluate to

$$\begin{aligned}\Gamma_{00}^0 &= -\frac{\Omega^2 \sin^2(\theta) (M - r^3 \Omega^2 \sin^2(\theta))}{\alpha^2} \\ \Gamma_{0r}^0 &= -\frac{(r^3 \Omega^2 \sin^2(\theta) - M) (\alpha^2 + r^2 \Omega^2 \sin^2(\theta))}{\alpha^4 r^2} \\ \Gamma_{rr}^0 &= \frac{\Omega^2 \sin^2(\theta) (-5M + r^3 \Omega^2 \sin^2(\theta) + 2r)}{\alpha^6} \\ \Gamma_{rr}^r &= \frac{\Omega^2 \sin^2(\theta) (-3M + r^3 \Omega^2 \sin^2(\theta) + r)}{\alpha^4} + \frac{2M^2}{r^3 \alpha^4} - \frac{M}{\alpha^4 r^2} \\ \Gamma_{0r}^r &= \frac{\Omega^2 \sin^2(\theta) (M - r^3 \Omega^2 \sin^2(\theta))}{\alpha^2} \\ \Gamma_{00}^r &= \frac{(r^3 \Omega^2 \sin^2(\theta) - M) (r^3 \Omega^2 \sin^2(\theta) - \alpha^2 r)}{r^3}\end{aligned}\tag{25}$$

The radial velocity now is

$$\beta_r = \alpha^2 \frac{\alpha^2 - \sin^2 \theta r^2 \Omega^2}{\frac{\alpha^2 \gamma_0}{\sqrt{\gamma_0^2 + \sin^2 \theta r^2 \Omega^2 - \alpha^2}} - \sin^2 \theta r^2 \Omega^2} = \begin{cases} \alpha^2 \left(1 - \frac{\alpha^2}{2\gamma_0^2}\right), & \gamma_0 \gg r\Omega \sin \theta \\ \alpha^2 \left(1 - \frac{1}{\sin^2 \theta r^2 \Omega^2} + \frac{\gamma_0}{\alpha^2 \sin^3 \theta r^3 \Omega^3}\right), & r \rightarrow \infty \end{cases}\tag{26}$$

Factors of α^2 in front are just relativistic coordinate time dilation for a particle moving in gravitational field.

3.4. Kerr black hole

In the equatorial plane we find

$$\beta_r = \frac{\alpha\sqrt{\Delta}\Delta_1 (r(\alpha^2 - \Delta_1\Omega^2) - 4aM^2\Omega)}{\gamma_0\sqrt{\frac{r(4a^2\Delta_1M^4r^2(\alpha^2 + \Delta_1\Omega^2) - 16a^3\Delta_1M^6r\Omega + 16a^4M^8 - 8a\alpha^2\Delta_1^2M^2r^3\Omega + \alpha^4\Delta_1^2r^4)}{4aM^2\Omega + r(-\alpha^2 + \gamma_0^2 + \Delta_1\Omega^2)}} + 4a^2M^4 - \Delta_1^2r^2\Omega^2} \quad (27)$$

For $r \rightarrow \infty$ we find

$$\beta_r = \alpha^2 - \frac{1 - a^2M^2\Omega^2/2}{r^2\Omega^2} + \frac{\gamma_0 + 4M\Omega(1 - aM\Omega/2)}{r^3\Omega^3} \quad (28)$$

It is understood that the solutions above involve both the kinematic effects of time-dilation (*e.g.* factor of α in front for the Schwarzschild case), as well as effects of centrifugal acceleration.

In conclusion, in all cases a particle moves radially with $\gamma \approx \gamma_0$ until $r\Omega \sim \gamma_0$. After that the wind acceleration takes over with $\gamma \sim r\Omega$.

3.5. Spiral with arbitrary radial step

The radial step of a magnetic spiral (denoted below $\equiv c/\Omega_1$) may be different from c/Ω , *e.g.*, the field may be affected by plasma inertia. For example, it is expected that inertial effects will make the spiral more tightly bound, larger $d\phi'$ for a given dr , hence $\Omega_1 \geq \Omega$. Equivalently, if the fast mode propagates with $\beta_s \leq 1$, in (3),

$$\begin{aligned} \beta_F &\rightarrow \beta_s\beta_F \\ \Omega_1 &= \frac{\Omega}{\beta_s} \geq \Omega \end{aligned} \quad (29)$$

Most importantly, the radial velocity of fast mode's propagation may change with radius depending on local plasma parameters. In this case the shape of the spiral is non-Archimedean. In our notations this implies radial dependence of the radial step: $\Omega_1(r)$.

Corresponding relations are fairly compact in Schwarzschild metric. Using

$$\begin{aligned} d\phi &\rightarrow d\phi' - \Omega dt \\ d\phi' &\rightarrow -\frac{\Omega_1}{\alpha^2} dr \end{aligned} \quad (30)$$

(instead of corresponding relations (5) with $\Omega_1 = \Omega$), we find

$$\beta_r = \frac{\alpha^2(\alpha^2 - r^2\Omega^2)}{\frac{\alpha\gamma_0\sqrt{\alpha^2 + r^2(\Omega_1^2 - \Omega^2)}}{\sqrt{-\alpha^2 + \gamma_0^2 + r^2\Omega^2}} - r^2\Omega\Omega_1} = \begin{cases} \alpha^2 \left(\frac{\alpha^2 - r^2\Omega^2}{\alpha\sqrt{\alpha^2 + r^2(\Omega_1^2 - \Omega^2)} - r^2\Omega\Omega_1} \right), & \gamma_0 \gg r\Omega \\ \alpha^2 \left(\frac{\Omega}{\Omega_1} - \frac{(\Omega_1 - \gamma_0\sqrt{\Omega_1^2 - \Omega^2})}{\alpha^2 r^2 \Omega_1^2 \Omega} \right), & r \rightarrow \infty \end{cases} \quad (31)$$

For flat space

$$\beta_r = \frac{1 - r^2\Omega^2}{\frac{\gamma_0\sqrt{1+r^2(\Omega_1^2-\Omega^2)}}{\sqrt{\gamma_0^2+r^2\Omega^2-1}} - r^2\Omega\Omega_1} = \begin{cases} \frac{1-r^2\Omega^2}{\sqrt{1+r^2(\Omega_1^2-\Omega^2)}-r^2\Omega\Omega_1} \left(1 - \frac{(1-r^2\Omega^2)\sqrt{r^2(\Omega_1^2-\Omega^2)+1}}{2\gamma_0^2(\sqrt{r^2(\Omega_1^2-\Omega^2)+1-r^2\Omega\Omega_1})} \right), & \gamma_0 \gg \Omega r \\ \frac{\Omega}{\Omega_1} - \frac{(\Omega_1 - \gamma_0\sqrt{\Omega_1^2 - \Omega^2})}{r^2\Omega_1^2\Omega}, & r \rightarrow \infty \end{cases} \quad (32)$$

Importantly, in the above relations the function $\Omega_1(r)$ is arbitrary, limited only by the condition $\Omega_1 \geq \Omega$. (So that a radial step per rotation can be smaller or equal to the light cylinder.

For given Ω and Ω_1 the toroidal velocity is

$$\beta_\phi = r\Omega \left(1 - \frac{\Omega_1}{\Omega} \beta_r \right) \quad (33)$$

Note that here Ω_1 may depend on radius r .

On physical grounds we expect $\Omega_1 \approx \Omega$. In other words, fast mode is nearly relativistic and plasma is nearly force-free. This is the intrinsic assumption of the model. For example, if $\Omega_1 = (1 + \delta_\Omega)\Omega$, $\delta_\Omega \ll 1$, then

$$\beta_\phi = r\Omega(1 - \beta_r + \delta_\Omega) \quad (34)$$

Thus, for Archimedean spiral with the radial step $1/\Omega$, a particle slightly overtakes the rotation pattern with the rate $\sim r\Omega(1 - \beta_r) \ll r\Omega$, while for $1 - \beta_r \ll \delta_\Omega$ a particle lags behind.

Thus, azimuthal velocity is small right from the light cylinder. Maximal toroidal velocity is $\sim 1/\gamma_0$, or $\sim \delta_\Omega$.

4. Numerical test

We have developed a Boris-based pusher (Boris & Roberts 1969; Birdsall & Langdon 1991). We verify the analytical results with direct integration, as we discuss below.

For Michel (1973) solution, consider a particle that in the wind frame (boosted by β_{EM} from the lab frame) moves with Lorentz factor γ'_0 (prime indicates Lorentz factor measured in the flow frame). Using electromagnetic velocity (1) and Lorentz transformations, we find the momentum in the lab frame p_{\parallel}

$$p_{\parallel} = \left\{ \frac{\beta'_0\gamma'_0 + (\gamma'_0 - 1)r^2\sin^2\theta\Omega^2}{\sqrt{1+r^2\sin^2\theta\Omega^2}}, 0, \frac{(\sqrt{1-\beta'_0} - \sqrt{\beta'_0+1})r\Omega\sin(\theta)}{\sqrt{\beta'_0+1}\sqrt{1+r^2\Omega^2\sin^2(\theta)}} \right\} \quad (35)$$

The momentum p_{\parallel} is that of a particle that is sliding along the local magnetic field with Lorentz factor γ'_0 as measured in the frame associated with β_{EM} (where electric field is zero). This is not a radial dependence, only a transformation at a given radius.

The total Lorentz factor is

$$\gamma = \gamma'_0 \sqrt{1 + \sin^2 \theta r^2 \Omega^2} = \sqrt{2} \gamma'_0 \quad (36)$$

a combination of parallel motion and orthogonal E-cross-B drift. The final relation in (36) applies to the light cylinder.

In Fig.4 we compare analytical results (18), and numerical integration - they are in excellent agreement.

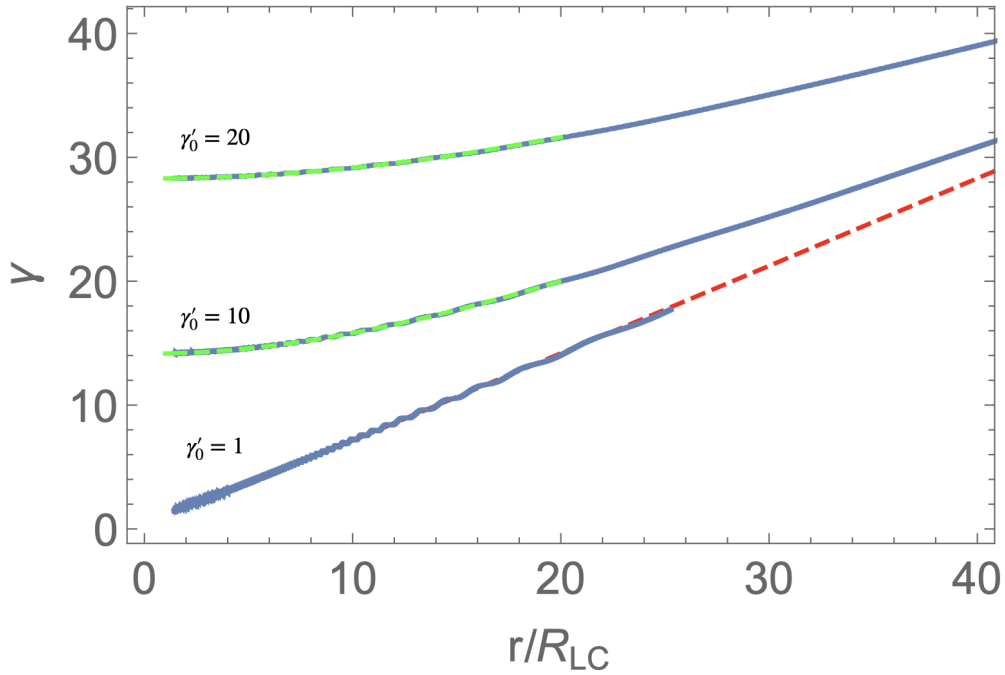


Fig. 6.— Direct integration of particle trajectories for the Lorentz factor of parallel motion $\gamma'_0 = 1, 10, 20$, $\theta = \pi/4$ (solid lines). The $\gamma'_0 = 1$ reproduces Michel's solution $\gamma = \sqrt{1 + r^2/2}$ (red dashed line). Green dashed lines: analytical solutions (18). In the simulations the magnetic field at the light cylinder satisfies $\omega_B = 10^4 \Omega$.

5. Jet in M87

5.1. Particle dynamics in parabolic magnetic field

In our model collimation is completely separated from acceleration in the vicinity of the light cylinder. To demonstrate this, let's choose prescribed collimated flow along parabolic flux surfaces

$$r(1 - \cos \theta) = \text{const} \quad (37)$$

In this case it is more convenient to work in cylindrical coordinates. The flux surface is then given by

$$z = \frac{\varpi^2 - r_0^2}{2r_0} \quad (38)$$

(ϖ is a cylindrical radial coordinate, r_0 is a parameter that marks a particular flux surface).

In the metric tensor we first change to the rotating frame, $d\phi \rightarrow d\phi' - \Omega dt$, add parabolic constraint $dz \rightarrow (\varpi/r_0)d\varpi$, and add a spiral step

$$\begin{aligned} d\phi' &= \Omega dl \\ dl &= \sqrt{1 + \varpi^2/r_0^2} d\varpi \end{aligned} \quad (39)$$

At each location the velocity in $\{\varpi, \phi, z\}$ coordinates is

$$\left\{ \beta_\varpi, \Omega\varpi \left(1 - \sqrt{1 + \frac{\varpi^2}{\varpi_0^2} \beta_\varpi} \right), \frac{\varpi\beta_\varpi}{\varpi_0} \right\} \quad (40)$$

Metric tensor in this case

$$\begin{aligned} G_{00} &= 1 - \Omega^2 \varpi^2 \\ G_{0\varpi} &= \Omega^2 \varpi^2 \sqrt{1 + \frac{\varpi^2}{\varpi_0^2}} \\ G_{\varpi\varpi} &= \left(1 + \frac{\varpi^2}{\varpi_0^2} \right) \Omega^2 \varpi^2 \end{aligned} \quad (41)$$

Following our procedure we find

$$\beta_\varpi = \frac{1 - (2\varpi - r_0) r_0 \Omega^2}{\frac{\gamma_0}{\sqrt{\frac{(2\varpi - r_0)(\gamma_0^2 + (2\varpi - r_0)r_0\Omega^2 - 1)}{(2\varpi - r_0)r_0^2\Omega^2 - 2\varpi}}} - (2\varpi - r_0) r_0 \Omega^2} \quad (42)$$

The resulting acceleration differs little from the case of conical flux surfaces of the Michel (1973) solution, Fig. 7

5.2. Emission maps

As we demonstrated above, particles injected from the black hole magnetosphere stream nearly along the magnetic flux surfaces - either conical for monopolar fields, parabolically, or more generally, along any given flux surface. The toroidal velocity remains small.

For a given shape of the magnetic flux surface (and some prescription for emissivity) we can then calculate the expected emission map. For monopolar magnetosphere any emission by relativistic radially moving particles will be centered on the source, the black hole.

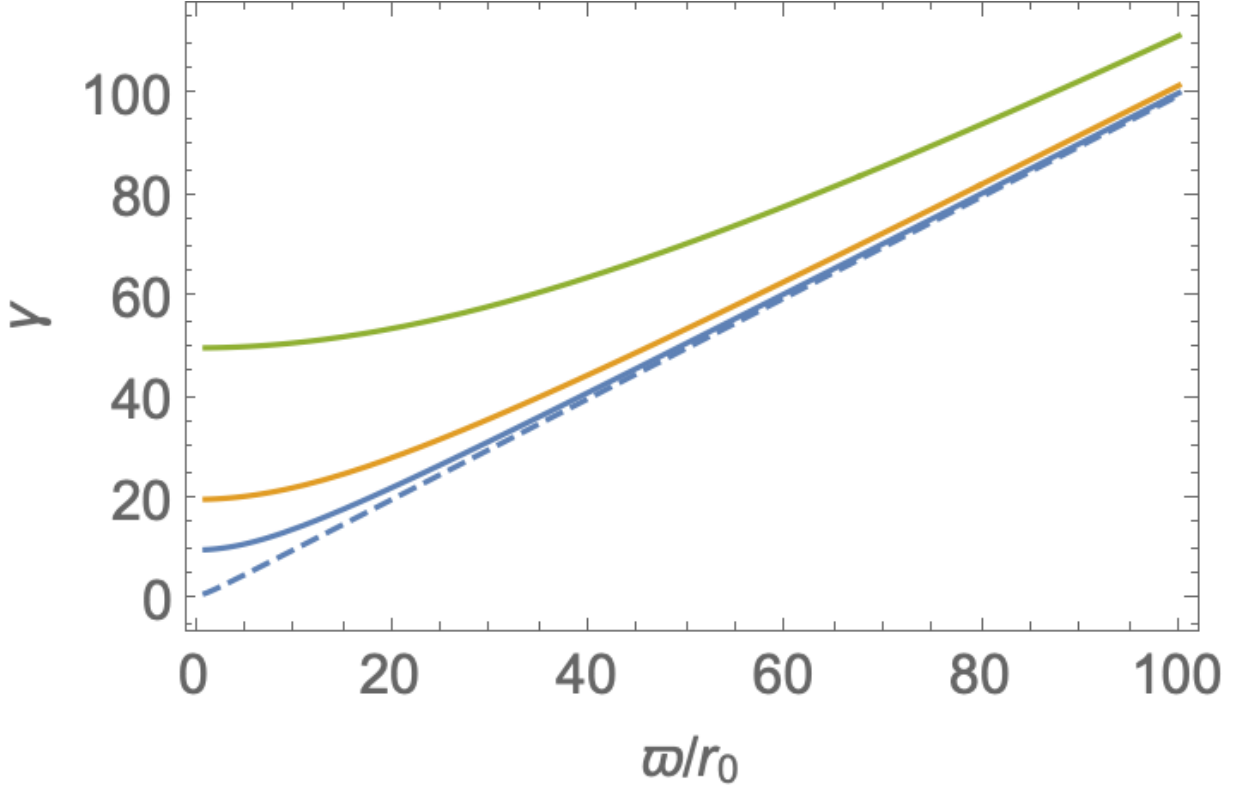


Fig. 7.— Lorentz factors of particles moving along parabolic spiral for different $\gamma_0 = 10, 20, 50$ (bottom to top curves). Dashed line is the Michel (1973) solution.

Even for curved flux surfaces, particles move with constant Lorentz factor almost purely along the flux surfaces, with minimal v_ϕ . For high injection Lorentz factors the emission will be dominated by the flow points when particle motion is aligned with the line of sight.

For example, for parabolical flux surfaces (Blandford & Znajek 1977), also Eq. (37), neglecting GR contribution, the line of sight can be parallel to a given flux surface emanating from the magnetosphere only if the lone of sight is $\theta_{ob} \leq \pi/4$. For smaller θ_{ob} , for a given flux surface parameterized by r_0 the tangent point is

$$\begin{aligned} \varpi_t &= r_0 \cot \theta_{ob} \\ z_t &= (\cot^2 \theta_{ob} - 1) \frac{r_0}{2} \end{aligned} \quad (43)$$

Choosing axis x_s on the plane of the sky along the projection of the spin of the black hole on the plane of the sky, the tangent point projects to

$$\begin{aligned} x_s &= \frac{r_0}{2 \sin \theta_{ob}} \\ y_s &= 0 \end{aligned} \quad (44)$$

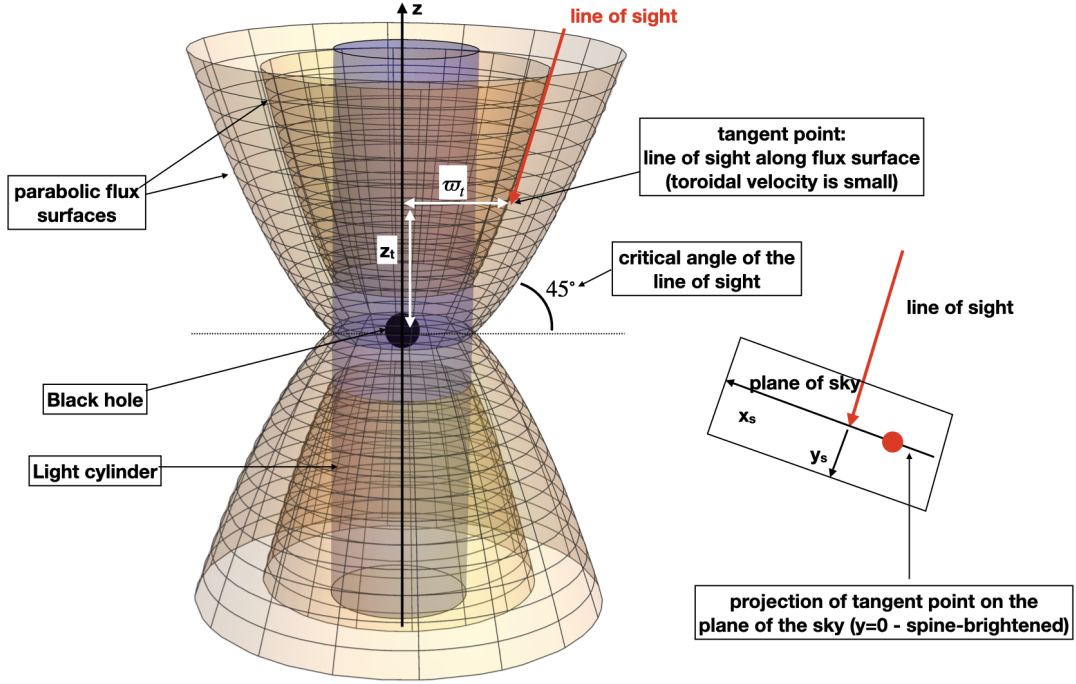


Fig. 8.— 3D rendering of parabolic magnetosphere. The vertical cylinder is the light cylinder. The insert on the right shows the sky image for a particular chosen line of sight. Due to high Doppler boosting the brightness peaks on the y axis - the spine.

Since the observed pattern is dominated by Lorentz boost, to calculate the images we employ the following procedure:

- Given the velocity (40-42) we calculate local Doppler factor δ . In fact, since toroidal velocity is small, one can use just the shape of the flux surface to find the local direction of the flow.
- We scale local density (somewhat arbitrary) as $1/r^2$, total spherical distance to the black hole.
- local emissivity is parameterized as

$$j \propto \frac{\delta^3}{r^2} \tag{45}$$

- emissivity is integrated along the line of sight.

In Fig. 10 we plot slices of the Doppler factor in the two orthogonal planes. Expected brightness maps are plotted in Figs. 11-13. All images, for any surface parameter r_0 , are spine-brightened. Hence any combination will be spine-brightened as well.

Finally, we conciliate emission from a possible current sheet outside of the light cylinder

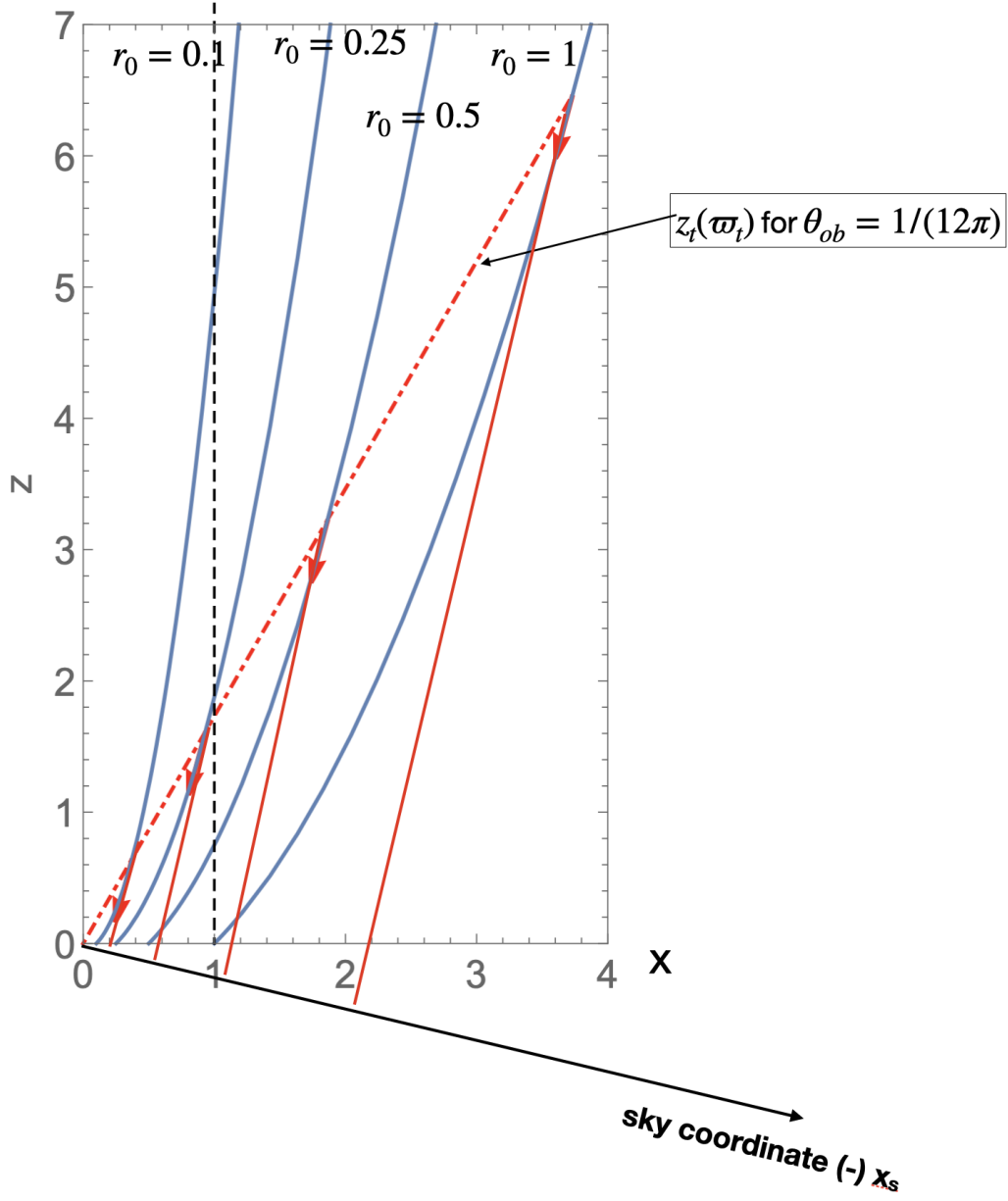


Fig. 9.— Parabolic magnetosphere and the lines of sight, $x - z$ cut. Solid lines are magnetic flux surface for $r_0 = 0.1, 0.25, 0.5, 1$. Red arrows start at points where the local line of sight is along the flux surface (hence maximal Doppler factor). Red dashed line, Eq. (44) - location of all such points. In this example $\theta_{ob} = \pi/12$. Coordinates are normalized to light cylinder radius.

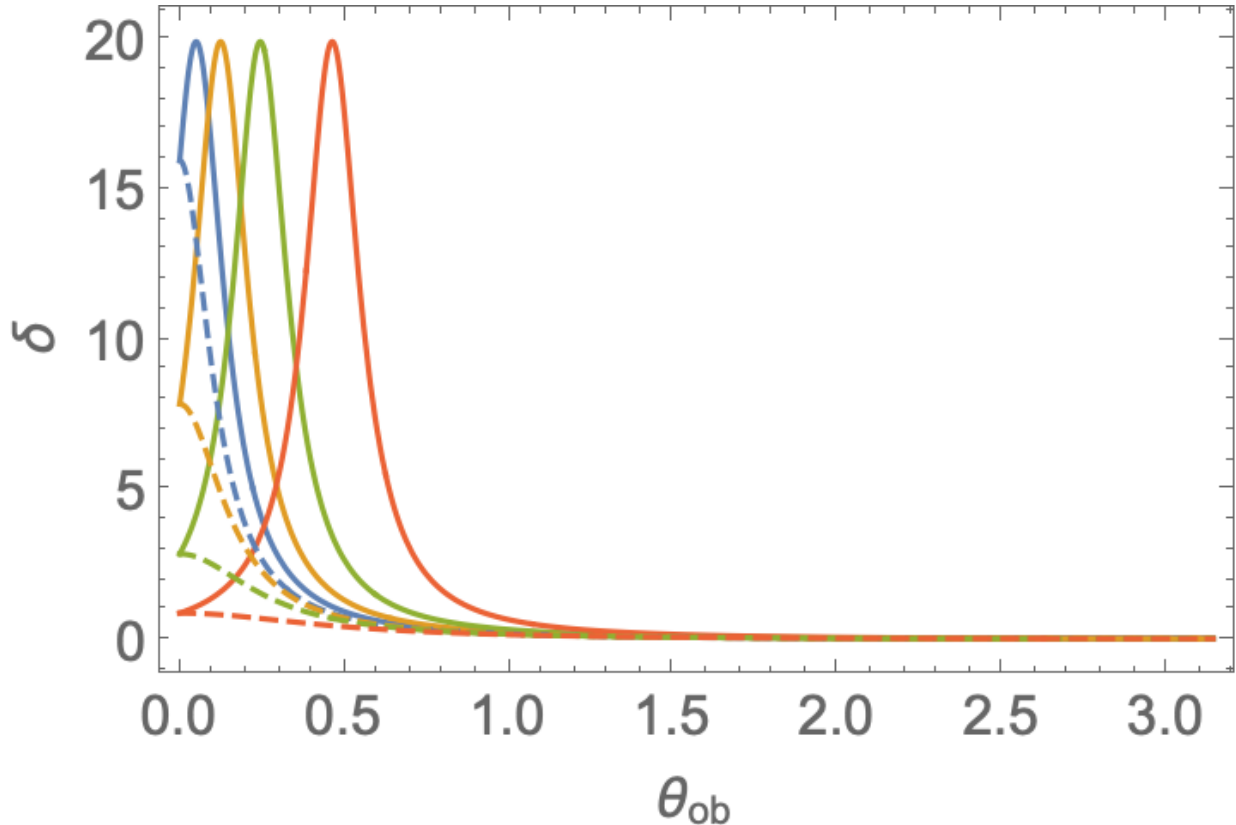


Fig. 10.— Doppler factor as a function of the observer angle θ_{ob} at $r = 2$. Slices are in the line-of-sight-black hole spin plane (solid lines) and in the orthogonal plane (dashed lines). Peaks in δ correspond to angles when the line-of-sight is tangential to the flux surface. Here and for the images below $\gamma_0 = 10$.

(Comisso & Asenjo 2021), by integrating the flux parameter r_0 from 1 to 2. The resulting structure is more elongated, more extended sideways, but is still spine-brightened, Fig. 14.

5.3. Conclusion: morphology of M87 jet and the BZ mechanism

Our results show a universal property of the resolved Blandford & Znajek (1977) flow with large parallel (to the local magnetic field) momentum of emitting particles: all images are spine-brightened, agreeing with what was observed. No special prescription for emissivity as function of the flux function parameter r_0 can change that: they are all spine-brightened. The assumption of parabolical flux surfaces is, naturally, an analytic approximation, yet the universality of the result - spine-brightened profile - ensures that it will be applicable to more general cases.

We then conclude that Blandford & Znajek (1977) mechanism is responsible for the M87

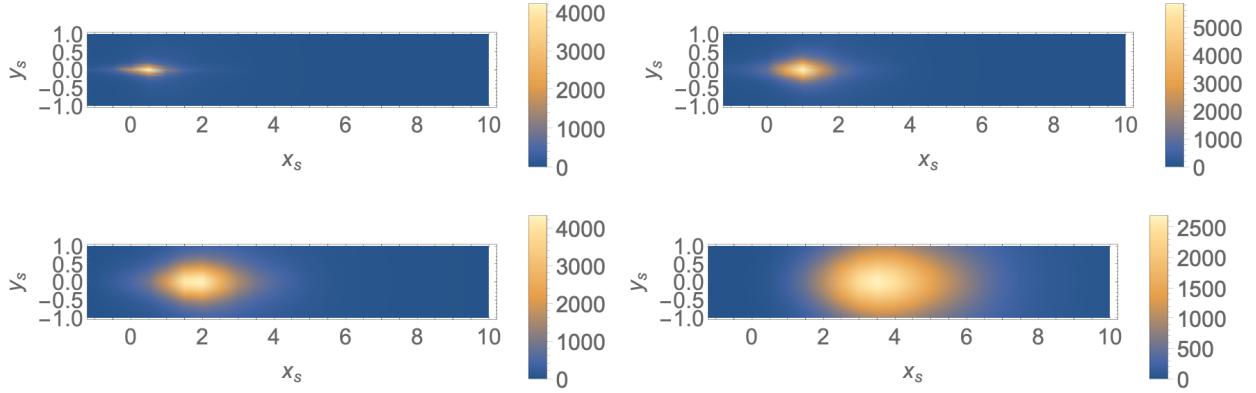


Fig. 11.— Image maps for $r_0 = 0.1, 0.25, 0.5, 1, \theta_{ob} = \pi/12$. The axes correspond to projected distances measured in terms of the light cylinder radius.

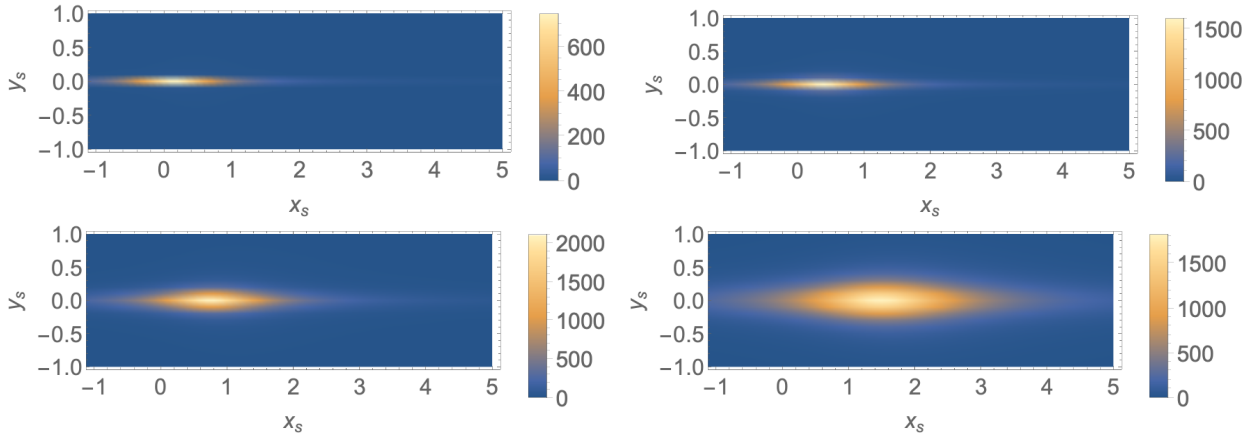


Fig. 12.— Image maps for $r_0 = 0.1, 0.25, 0.5, 1, \theta_{ob} = \pi/6$.

jet, at least in its pure form. **By *BZ mechanism* we understand generation of collimated relativistic jet. The relativistic e^\pm we describe do extract energy from the spin of the black hole.**

The Blandford & Znajek (1977) mechanism can still be operational - and, *e.g.* responsible for the bright core in the images of M87 in case of purely radial outflow at small r , but it does not drive the observed jet. Another possibility is that the sheath is slowed down by the interaction with the disk corona - while the core remains relativistic, with emission beamed away. This would correspond to emission coming only from small r_0 , top rows in Figs. 11 and 12 - it is still spine-brightened, but shows only in the small part of the image.

In contrast disk-produced outflows (Blandford & Payne 1982) start non-relativistically. The extended structure observed in M87 is thus inconsistent with the magnetosphere-produced jet, but

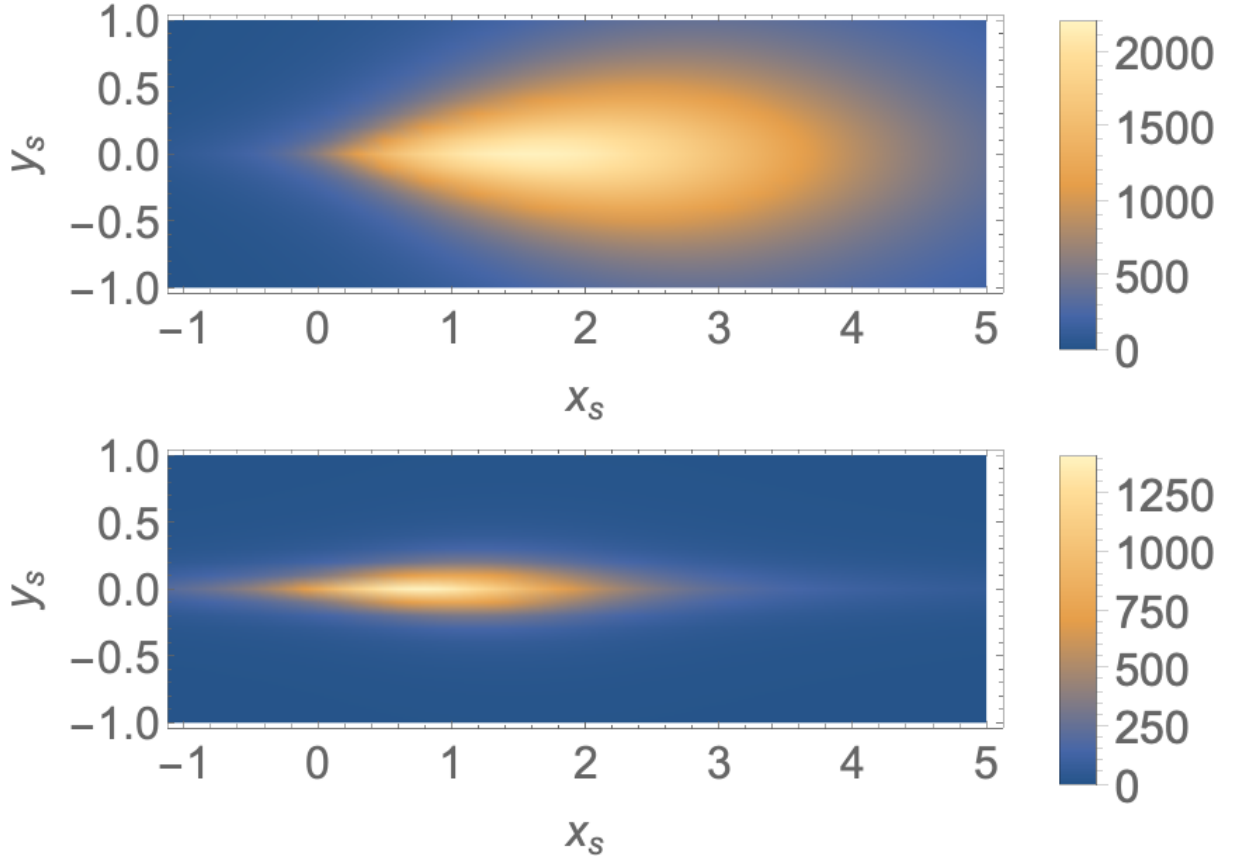


Fig. 13.— Image maps integrated over $0 \leq r_0 \leq 1$ for $\theta_{ob} = \pi/12$ (top panel) and $\theta_{ob} = \pi/6$ (bottom panel). Larger r_0 corresponds to flux surfaces not emanating from the magnetosphere.

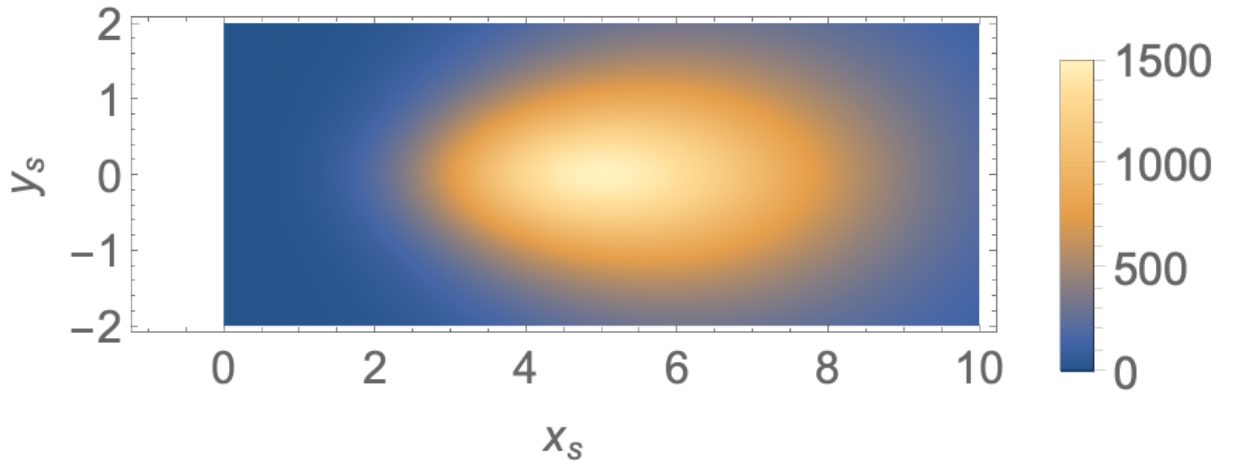


Fig. 14.— Emission pattern from the outside current sheet, $1 \leq r_0 \leq 2$

is consistent with the disk-produce jets.

On larger scales, of the order of parsecs, in the grand spiral paradigm of a jet moving with Lorentz factor of \sim few Lyutikov et al. (2005), the edge-brightened jet is actually expected on theoretical grounds (*e.g.* Fig. 1 of Clausen-Brown et al. 2011). In addition, asymmetries across the jet in intensity, polarization and spectral index maps are expected.

5.4. Plasma dynamics and pair production in force-free and PIC simulations

Two approaches are commonly used to study relativistic winds and jets: force-free simulation (Spitkovsky 2006, *e.g.*) and PIC simulations (*e.g.* Chen & Beloborodov 2014; Philippov et al. 2015; Crinquand et al. 2020; Hakobyan et al. 2022; Ripperda et al. 2022).

In ideal force-free simulation the velocity along the field is not defined in principle. (Inclusion of resistivity in the force-free approach requires some choice of parallel velocity Lyutikov (2003); Gruzinov (2007).) Thus the effects discussed here are completely missed in force-free simulation.

In case of PICs the effects of initial large injection Lorentz factor are missed by choice (see though Crinquand et al. 2020). To simulate pair production in PICs typically some kind of prescription is employed: either a density floor, or a condition on the value of the local electric field. According to a given prescription pairs are added *at rest* (except in Crinquand et al. 2020). Instead, they should be added with large Lorentz factors. If the number of added pairs is comparable to the initial one, the resulting structure of the magnetosphere will be drastically different.

Our results have implications for PIC simulations (that the newly born e^\pm pairs should be injected with large initial Lorentz factor), and interpretation of the images of black holes by the Event Horizon Telescope.

This is a qualitatively different set-up from what the conventional black hole acceleration models assume. Jets start fast, with Lorentz factor $\gg 1$. At first they carry small power. Only later on the magnetic field acceleration takes over.

6. Discussion

We demonstrate that outflows produced within magnetospheres of neutron stars and black holes start relativistically right from within the light cylinder. To produce jets the overall magnetic field just needs to collimate the outflow - acceleration is already achieved by injection. For highly magnetized flows with $\sigma \gg 1$ the kinetic luminosity of the jet is $L_k \sim L_P/\sigma \leq L_P$, when L_P is the Poynting power, but the jet is already relativistic. It can be further accelerated by the magnetic forces beyond $r\Omega \sim \gamma_0$.

Any signal produced by radially moving particles with $\gamma \gg 1$ will be centered on the source.

For parabolic flux surfaces we calculated the expected images - they are all spin-brightened, in agreement to observations of M87 jet. We then conclude that M87 jet can be produced with the black hole magnetosphere by the BZ mechanism.

Finally, we point out that in PIC simulations pairs must be injected relativistically - this will change the overall structure of both pulsar and black holes magnetospheres.

Acknowledgments

This work had been supported by NASA grant 80NSSC18K064 and NSF grants 1903332 and 1908590. We would like to thank Nahum Arav, Maxim Barkov, Vasily Beskin, Ioannis Contopoulos, Hayk Hakobyan, Sergey Komissarov, Mikhilail Medvedev, Frank Rieger, Markek Sikora, Elena Nokhrina for comments, and organizers of the IAU conference "Black Hole Winds at all Scales" for hospitality.

7. Data availability

The data underlying this article will be shared on reasonable request to the corresponding author.

REFERENCES

- Bardeen, J. M., Press, W. H., & Teukolsky, S. A. 1972, *ApJ*, 178, 347
- Barkov, M. V., & Komissarov, S. S. 2008, *MNRAS*, 385, L28
- Beskin, V. S. 2009, *MHD Flows in Compact Astrophysical Objects: Accretion, Winds and Jets*
- Beskin, V. S., Istomin, Y. N., & Porev, V. I. 1992, *Soviet Ast.*, 36, 642
- Beskin, V. S., & Kuznetsova, I. V. 2000, *Nuovo Cimento B Serie*, 115, 795
- Bicknell, G. V., & Begelman, M. C. 1996, *ApJ*, 467, 597
- Birdsall, C. K., & Langdon, A. B. 1991, *Plasma Physics via Computer Simulation*
- Blandford, R., Meier, D., & Readhead, A. 2019, *ARA&A*, 57, 467
- Blandford, R. D., & Königl, A. 1979, *ApJ*, 232, 34
- Blandford, R. D., & Payne, D. G. 1982, *MNRAS*, 199, 883
- Blandford, R. D., & Znajek, R. L. 1977, *MNRAS*, 179, 433

- Boris, J. P., & Roberts, K. V. 1969, *Journal of Computational Physics*, 4, 552
- Camenzind, M. 1986, *A&A*, 162, 32
- Chen, A. Y., & Beloborodov, A. M. 2014, *ApJ*, 795, L22
- Clausen-Brown, E., Lyutikov, M., & Kharb, P. 2011, *MNRAS*, 415, 2081
- Comisso, L., & Asenjo, F. A. 2021, *Phys. Rev. D*, 103, 023014
- Contopoulos, I., Pétri, J., & Stefanou, P. 2020, *MNRAS*, 491, 5579
- Crinquand, B., Cerutti, B., Philippov, A., Parfrey, K., & Dubus, G. 2020, *Phys. Rev. Lett.*, 124, 145101
- Goldreich, P., & Julian, W. H. 1970, *ApJ*, 160, 971
- Grad, H. 1967, *Physics of Fluids*, 10, 137
- Gralla, S. E., & Jacobson, T. 2014, *MNRAS*, 445, 2500
- Gruzinov, A. 2007, arXiv e-prints, arXiv:0710.1875
- Hakobyan, H., Philippov, A., & Spitkovsky, Anatoly, *et al.* 2022, arXiv e-prints, arXiv:2209.02121
- Hirovani, K., & Okamoto, I. 1998, *ApJ*, 497, 563
- Kim, J. Y., Krichbaum, T. P., & Lu, R. S., *et al.* 2018, *A&A*, 616, A188
- Komissarov, S. S. 2004, *MNRAS*, 350, 427
- Komissarov, S. S., Vlahakis, N., Königl, A., & Barkov, M. V. 2009, *MNRAS*, 394, 1182
- Krolik, J. H. 1999, *Active galactic nuclei : from the central black hole to the galactic environment*
- Landau, L. D., & Lifshitz, E. M. 1975, *The classical theory of fields*
- Levinson, A. 2000, *Phys. Rev. Lett.*, 85, 912
- Levinson, A., & Rieger, F. 2011, *ApJ*, 730, 123
- Lu, R.-S., Asada, K., & Krichbaum, Thomas P, *et al.* 2023, *Nature*, 616, 686
- Lyutikov, M. 2003, *MNRAS*, 346, 540
- . 2009, *MNRAS*, 396, 1545
- . 2022, *ApJ*, 933, L6
- Lyutikov, M., Pariev, V. I., & Gabuzda, D. C. 2005, *MNRAS*, 360, 869

- McKinney, J. C. 2006, MNRAS, 368, 1561
- Michel, F. C. 1969, ApJ, 158, 727
- . 1973, ApJ, 180, L133
- Misner, C. W., Thorne, K. S., & Wheeler, J. A. 1973, Gravitation (San Francisco: W.H. Freeman and Co., 1973)
- Nakamura, M., & Asada, K. 2013, ApJ, 775, 118
- Nokhrina, E. E., & Beskin, V. S. 2017, MNRAS, 469, 3840
- Philippov, A. A., Spitkovsky, A., & Cerutti, B. 2015, ApJ, 801, L19
- Prokofev, V. V., Arzamasskiy, L. I., & Beskin, V. S. 2018, MNRAS, 474, 1526
- Ptitsyna, K., & Neronov, A. 2016, A&A, 593, A8
- Ripperda, B., Liska, M., & Chatterjee, K., *et al.* 2022, ApJ, 924, L32
- Scharlemann, E. T., & Wagoner, R. V. 1973, ApJ, 182, 951
- Shafranov, V. D. 1966, Reviews of Plasma Physics, 2, 103
- Spitkovsky, A. 2006, ApJ, 648, L51
- Tomimatsu, A. 1994, PASJ, 46, 123

A. Constrained motion in flat space

Here we aim to re-derive the results for flat metric using Lagrangian and Hamiltonian approaches for constrained motion in flat space.

Consider relativistic particle moving along rotating spiral in cylindrical coordinates in flat space. One possible choice of relativistic Lagrangian is (Landau & Lifshitz 1975)

$$\mathcal{L} = -\sqrt{1 - \beta_\phi^2 - \beta_r^2} \tag{A1}$$

(see also Appendix B for an alternative choice).

The field lines of the Michel's solution are given as a parametric curve in $x - y - z$ coordinates (at any moment t)

$$\begin{aligned} \mathcal{C} &: \{r \sin(\theta) \cos(\phi), r \sin(\theta) \sin(\phi), r \cos(\theta)\} \\ \phi &= (t - r)\Omega \end{aligned} \tag{A2}$$

where spherical r is a parameter along the curve, Fig. 15.

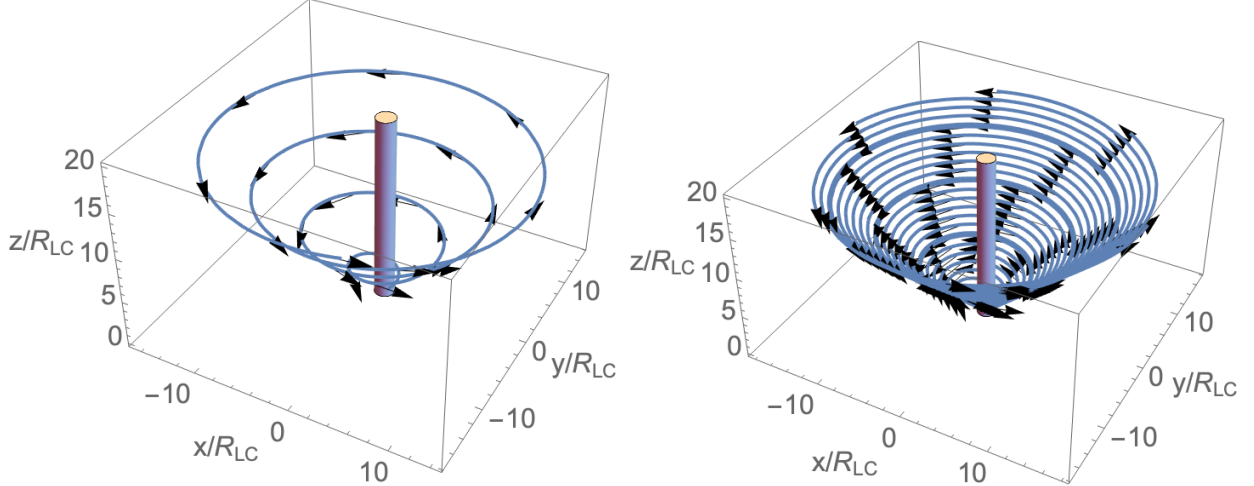


Fig. 15.— Field lines for Michel's solution.

Total velocity (differentiating (A2) with respect to time)

$$\mathbf{v} = \beta_r \mathbf{e}_r + \sin \theta r \Omega (1 - \beta_r) \mathbf{e}_\phi \tag{A3}$$

The Lagrangian then becomes

$$\mathcal{L} = -\sqrt{1 - \beta_r^2 - \sin^2 \theta r^2 \Omega^2 (1 - \beta_r)^2} \tag{A4}$$

($\theta = \pi/2$ is assumed below for simplicity).

Lagrange equation for coordinate r with $\beta_r = \partial_t r$

$$\partial_r \mathcal{L} = \partial_t (\partial_{\beta_r} \mathcal{L}) \tag{A5}$$

gives

$$\partial_t \beta_r = r \Omega^2 (1 - \beta_r)^2 (1 - r^2 \Omega^2 + \beta_r (2 + r^2 \Omega^2)) \tag{A6}$$

Solution satisfying $r(t = 0) = 1/\Omega$ is

$$t = r - \frac{1}{\Omega} + \frac{\log \left(\frac{(\gamma_0^2 - 1)(r\Omega - 1)(\sqrt{\gamma_0^2 + r^2 \Omega^2 - 1} + \gamma_0 r \Omega)}{\gamma_0^2 (r\Omega + 1)(\gamma_0 r \Omega - \sqrt{\gamma_0^2 + r^2 \Omega^2 - 1})} \right)}{2\Omega} \tag{A7}$$

where the integration constant γ_0 was chosen to match (17). Differentiating (A7) with respect to time we recover (17).

As a check, let us repeat the above derivation using Hamiltonian approach. Given Lagrangian (A4) we can find canonical momentum P_r and Hamiltonian

$$\begin{aligned} P_r &= \partial_{\beta_r} \mathcal{L} = \frac{\beta_r - r^2 \Omega^2 (1 - \beta_r)}{\sqrt{1 - \beta_r^2 - r^2 \Omega^2 (1 - \beta_r)^2}} \\ \mathcal{H} &= \beta_r P_r - \mathcal{L} = \frac{r^2 \Omega^2 P_r + \sqrt{P_r^2 + r^2 \Omega^2 + 1}}{r^2 \Omega^2 + 1} \end{aligned} \quad (\text{A8})$$

Canonical equations are then

$$\begin{aligned} \beta_r &= \partial_t r = \partial_{P_r} \mathcal{H} = \frac{r^2 \Omega^2}{1 + r^2 \Omega^2} + \frac{P_r}{(1 + r^2 \Omega^2) \sqrt{1 + P_r^2 + (r\Omega)^2}} \\ \partial_t P_r &= -\partial_r \mathcal{H} = \frac{r \Omega^2 \left(-2P_r \sqrt{P_r^2 + r^2 \Omega^2 + 1} + 2P_r^2 + r^2 \Omega^2 + 1 \right)}{(r^2 \Omega^2 + 1)^2 \sqrt{P_r^2 + r^2 \Omega^2 + 1}} \end{aligned} \quad (\text{A9})$$

Equating $\mathcal{H} = \gamma_0$ we find

$$P_r = \frac{\gamma_0 r^2 \Omega^2 + \sqrt{\gamma_0^2 + r^2 \Omega^2 - 1}}{1 - r^2 \Omega^2} \quad (\text{A10})$$

Using (A10) in expression for velocity (A9) we recover (17).

The Lagrangian approach requires integration of the equations of motion and allows one to find $r(t)$, while the more simple Hamilton-Jacobi approach, which involves only algebraic relations, gives only $\beta_r(r)$. This is sufficient for our application.

B. Another Lagrangian approach in Schwarzschild metric

Let us next extend the results of Appendix A to Schwarzschild metric using a somewhat different approach. We are interested in getting the radial speed of the particle along the string (i.e., on the (1+1)-D manifold). The alternative choice of Lagrangian is

$$\mathcal{L}(\dot{t}, \dot{r}, r) = \frac{1}{2} [-G_{00} \dot{t}^2 + G_{rr} \dot{r}^2 + 2G_{0r} \dot{t} \dot{r}], \quad \dot{x} = \frac{dx}{d\tau} \quad (\text{B1})$$

From the symmetry of the Lagrangian in the t coordinate, we use the Euler-Lagrange equation to get

$$\dot{t} = \frac{G_{0r} \dot{r} + E}{G_{00}}, \quad G_{00} \neq 0 \quad (\text{B2})$$

where E is a constant of motion. It is generally different from γ_0 - different choices of the Lagrangian result in different integration constants; the exact relations between different constants are typically complicated.

For timelike trajectories,

$$\mathcal{L}(\dot{r}, r) = \frac{1}{2} \left[\left(G_{rr} + \frac{G_{0r}^2}{G_{00}} \right) \dot{r}^2 - \frac{E^2}{G_{00}} \right] = -\frac{1}{2} \quad (\text{B3})$$

The speed of the coordinate r with respect to the proper time (the time measured by the particle that is constrained to move along the string) is

$$\dot{r} = \pm \sqrt{\frac{E^2 - G_{00}}{G_{0r}^2 + G_{00} G_{rr}}} \quad (\text{B4})$$

The sign here determines the direction of motion: either towards or away from the black hole. The speed of the coordinate r with respect to the coordinate t is

$$\beta_r = \frac{dr}{dt} = \frac{\dot{r}}{\dot{t}} \stackrel{(\text{B2})}{=} G_{00} \left(G_{0r} + \frac{E}{\dot{r}} \right)^{-1} = G_{00} \left(G_{0r} \pm E \sqrt{\frac{G_{0r}^2 + G_{00} G_{rr}}{E^2 - G_{00}}} \right)^{-1} \quad (\text{B5})$$

This recovers equation (14), obtained by the Hamilton-Jacobi approach.

Consider rotating magnetosphere in Schwarzschild metric. We use the following convention

$$G_{00} = \alpha^2 - r^2 \Omega^2, \quad G_{rr} = \frac{1}{\alpha^2} + \frac{r^2 \Omega^2}{\alpha^4}, \quad G_{0r} = -\frac{r^2 \Omega^2}{\alpha^2} \quad (\text{B6})$$

The Lagrangian is then

$$\mathcal{L} = \frac{1}{2} \left(-\alpha^2 \left(1 - \frac{r^2 \Omega^2}{\alpha^2} \right) \dot{t}^2 + \frac{1}{\alpha^2} \left(1 + \frac{r^2 \Omega^2}{\alpha^2} \right) \dot{r}^2 - 2 \frac{r^2 \Omega^2}{\alpha^2} \dot{t} \dot{r} \right) \quad (\text{B7})$$

Between the two light cylinders, the constant of motion

$$E = (\alpha^2 - r^2 \Omega^2) \dot{t} + \frac{r^2 \Omega^2}{\alpha^2} \dot{r} \quad (\text{B8})$$

We then get \dot{r} by substituting in (B4) or by solving the quadratic equation (B7) using $G_{00} G_{rr} + G_{0r}^2 = 1$ (in our case):

$$\dot{r} = \frac{-G_{0r} \dot{t} \pm \sqrt{\dot{t}^2 - G_{rr}}}{G_{rr}} \quad (\text{B9})$$

Eliminating \dot{t} with (B8),

$$\dot{t} = \frac{\alpha^2 E - r^2 \Omega^2 \dot{r}}{\alpha^2 (\alpha^2 - r^2 \Omega^2)} \quad (\text{B10})$$

we find Lagrangian and Hamiltonian

$$\begin{aligned}\mathcal{L} &= \frac{\dot{r}^2 - E^2}{2(\alpha^2 - r^2\Omega^2)} \\ \mathcal{H} = \dot{r}\partial_{\dot{r}}\mathcal{L} - \mathcal{L} &= \frac{\dot{r}^2 + E^2}{2(\alpha^2 - r^2\Omega^2)}\end{aligned}\tag{B11}$$

We used ($\sqrt{2}$ times) the proper time to parameterize the Lagrangian in (B7); thus, the Lagrangian has a constant value of $-1/2$ with this parameterization for timelike geodesics. Therefore, \dot{r} is

$$\dot{r} = \pm\sqrt{r^2\Omega^2 + E^2 - \alpha^2},\tag{B12}$$

consistent with (22).

The radial velocity measured by the coordinate time of the observer is then

$$\beta_r = \frac{\dot{r}}{\dot{t}} = \frac{\alpha^2(\alpha^2 - r^2\Omega^2)}{\frac{\alpha^2 E}{\sqrt{r^2\Omega^2 + E^2 - \alpha^2}} - r^2\Omega^2}\tag{B13}$$

The geodesic equation takes a nice form

$$\ddot{r} = \frac{1}{2}\frac{d}{dr}(\dot{r}^2) = r\Omega^2 - \frac{M}{r^2},\tag{B14}$$

(derivatives are with respect to proper time) which unites the cases of radial motion in Schwarzschild geometry (*e.g.* Misner et al. 1973) and (22).

We also note that one can get the same differential equation (for the case between the two light cylinders) by solving the classical mechanical problem of a particle with mass m constrained to move along a straight wire rotating with a constant angular speed Ω in the flat 2-D plane, with the inclusion of a source of mass M at the center. The Lagrangian is ($\dot{r} = dr/dt$)

$$\mathcal{L} = \frac{1}{2}m(\dot{r}^2 + r^2\Omega^2) - U(r), \quad U(r) = -m\frac{MG}{r}\tag{B15}$$

C. Limitations on angular velocity of field lines

Transformation to the rotating Kerr metric has limitations (Lyutikov 2009): it is physical only for angular velocities smaller than ω_{ph} , angular velocity of a photon orbit, defined by the conditions of circular rotation with the speed of light $g_{00} = 0$, $\partial_r g_{00} = 0$. This gives $-4a^2M + r(-3M + r)^2 = 0$ (Bardeen et al. 1972). For a given a and r , the transformation to the rotating Kerr metric becomes meaningless for ω higher than the angular velocity of a photon circular orbit,

$$\omega_{ph} = \frac{1}{\mp|a| + 6M \cos(\frac{1}{3}\arccos(\mp|a|/M))}\tag{C1}$$

The upper sign corresponds to prograde rotation. Particular values are $a = 0$, $r_{\text{ph}} = 3M$, $\omega_{\text{ph}} = 1/(3\sqrt{3}M)$ for Schwarzschild black hole, $a = M$, $r_{\text{ph}} = M$, $\omega_{\text{ph}} = 1/(2M)$ for prograde and $a = -M$, $r_{\text{ph}} = 4M$, $\omega_{\text{ph}} = 1/(7M)$ for retrograde photon orbits. For $1/(7M) < \omega < 1/(2M)$ this requires sufficiently high a , satisfying $\omega < 1/(a + 2\sqrt{2}M(1 + \cos(\frac{2}{3}\arccos(-\frac{a}{M}))))^{3/2}$ (for $a = 0$ this requires $\omega < 1/(3\sqrt{3})$). For $\omega \rightarrow 1/(2M)$ both light cylinders merge on the black hole horizon at $a = M = r$. For higher ω , the transformation to the rotating frame becomes meaningless everywhere (Fig. 16).

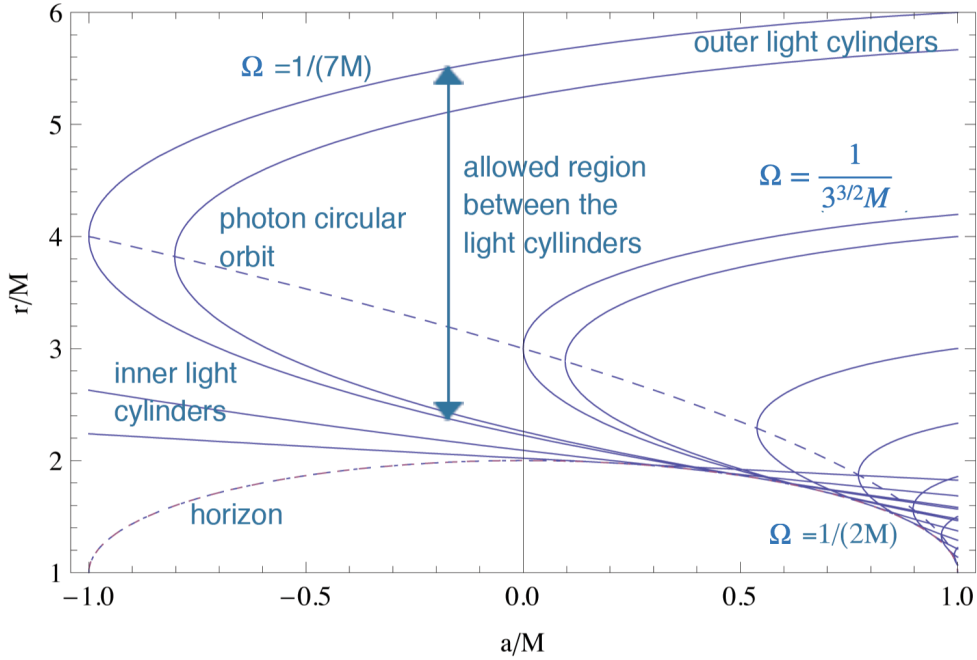


Fig. 16.— The locations of light cylinders for different ω as function of a . The light cylinders always lie outside the horizon (dotted curve). For a given ω , the inner and outer light cylinders merge at the photon circular orbit (dashed line). The physically meaningful region lies in between the light cylinders, to the right of the light cylinders curve. For $\omega \rightarrow 0$, the inner light cylinder coincides with the ergosphere $r = 2M$. As ω increases, the outer light cylinder moves to smaller r ; the radial location of the inner light cylinder is a complicated function of ω . For $\omega > 1/(7M)$ there is a region for sufficiently small a , for which the transformation to the rotating frame is unphysical. For high $\omega \rightarrow 1/(2M)$ and high $a > M/\sqrt{2}$, the inner light cylinder moves inside the ergosphere of a Kerr black hole. For $\omega > 1/(2M)$, the transformation to rotating frame is unphysical everywhere. Adapted from (Lyutikov 2009)

D. Kerr Black Hole Analysis

In this Appendix, we calculate the velocity components relative to an observer at infinity and show that the radial component dominates in a few light cylinder radii; we also obtain the Lorentz factor of the speed relative to both fixed observers in spacetime and co-rotating observers with the field lines.

We consider a (2+1)-D manifold of the Kerr black hole with a constant θ . Then, we move to a (1+1)-D sub-manifold that is rotating with a constant angular speed Ω according to

$$d\phi = \Phi'(r) dr + \Omega dt \quad \Phi'(r) = \frac{d\Phi(r)}{dr} \quad (\text{D1})$$

This means that a particle in this sub-manifold is constrained to move along a wire with a shape function $\Phi(r)$. Using the formula in (5), we define the wire function as follows:

$$\Phi'(r) = \omega_{sp} = -\sqrt{\frac{g_{rr}}{g_{00}}} \left(\frac{g_{0\phi}}{g_{\phi\phi}} + \Omega_1(r) \right) \quad (\text{D2})$$

where $\Omega(r)$ is a function of the radial coordinate as a generalization of the Archimedean spiral shape (e.g., $\Omega_1(r) = \Omega$ is the Archimedean spiral case). We note from (31) that this function has some constraints to have a physically realizable spiral step (like in the Schwarzschild metric, $\Omega_1(r) \geq \Omega$). Using the notation in (7), the metric of is

$$\begin{aligned} ds^2 &= -G_{00} dt^2 + G_{rr} dr^2 + 2G_{0r} dt dr \\ G_{00} &= g_{00} - (\Omega g_{\phi\phi} + 2g_{0\phi})\Omega \\ G_{rr} &= g_{rr} + \Phi'(r)^2 g_{\phi\phi} \\ G_{0r} &= (\Omega g_{\phi\phi} + g_{0\phi}) \Phi'(r) \end{aligned} \quad (\text{D3})$$

Note that we have constraints on the values of the mass-rotation parameter $\eta = M\Omega$ and the Kerr parameter a :

$$\eta \sqrt{\frac{(1-a\eta)}{(1+a\eta)^3}} < \frac{1}{3\sqrt{3}} \quad (\text{D4})$$

In the Kerr case, we have (by definition) the following coordinate basis vectors

$$(\mathbf{e}_0)^\mu = \begin{pmatrix} 1 \\ 0 \\ 0 \end{pmatrix} \quad (\mathbf{e}_r)^\mu = \begin{pmatrix} 0 \\ 1 \\ 0 \end{pmatrix} \quad (\mathbf{e}_\phi)^\mu = \begin{pmatrix} 0 \\ 0 \\ 1 \end{pmatrix} \quad (\text{D5})$$

Of course, these basis vectors satisfy $\mathbf{e}_\mu \cdot \mathbf{e}_\nu = g_{\mu\nu}$. The lengths are

$$|\mathbf{e}_\mu| = \sqrt{g_{\mu\mu}} \quad \Rightarrow \quad |\mathbf{e}_0| = \sqrt{-g_{00}} \quad |\mathbf{e}_r| = \sqrt{g_{rr}} \quad |\mathbf{e}_\phi| = \sqrt{g_{\phi\phi}} \quad (\text{D6})$$

To get the velocity components, we need to take the total (intrinsic) derivative of the normalized position vector components \hat{V}^μ (note $v^\mu := dx^\mu/dt$)

$$\frac{D}{Dt}\hat{V}^\mu = |\mathbf{e}_\mu| \left[\frac{d}{dt} \left(\frac{\hat{V}^\mu}{|\mathbf{e}_\mu|} \right) + \left(\Gamma_{\alpha\beta}^\mu v^\beta \right) \left(\frac{\hat{V}^\alpha}{|\mathbf{e}_\alpha|} \right) \right] \quad (\text{D7})$$

We obtain the velocity components as follows

1. The radial component β_r

$$\beta_r = \frac{D}{Dt}\hat{V}^r = \frac{D}{Dt}r = v^r \left(1 + r \left(\frac{1}{2} \frac{d}{dr} \ln(g_{rr}) - \frac{1}{2} \frac{d}{dr} \ln(g_{rr}) \right) \right) = v^r \quad (\text{D8})$$

Thus, we are right about our calculations that

$$\beta_r = \frac{Dr}{Dt} = \frac{dr}{dt} \quad (\text{D9})$$

2. The azimuthal component

$$\beta_\phi = \frac{D}{Dt}\hat{V}^\phi = \frac{\sqrt{g_{rr}g_{\phi\phi}}}{2r \sin^2 \theta} \left[g_{00}^2 \frac{d}{dr} \left(\frac{g_{0\phi}}{g_{00}} \right) + [\beta_r \Phi'(r) + \Omega] \left(g_{00} \frac{dg_{\phi\phi}}{dr} + g_{0\phi} \frac{dg_{0\phi}}{dr} \right) \right] \quad (\text{D10})$$

The velocity vector can be written as (still working in the normalized basis)

$$\mathbf{v} = \beta_r \hat{\mathbf{e}}_r + \beta_\phi \hat{\mathbf{e}}_\phi \quad (\text{D11})$$

In the case of the Schwarzschild metric ($a = 0$),

$$\Phi'(r) = -\frac{\Omega_1(r)}{\alpha^2} \quad (\text{D12})$$

The velocity vector is (see how it reduces to the flat spacetime case in (A3) when we have Archimedean spiral, $\Omega_1(r) = \Omega$)

$$\mathbf{v} = \beta_r \mathbf{e}_r + r\Omega \left(\alpha - \frac{1}{\alpha} \frac{\Omega_1(r)}{\Omega} \beta_r \right) \mathbf{e}_\phi \quad \xrightarrow[\alpha=1]{M=0} \quad \mathbf{v} = \beta_r \mathbf{e}_r + r\Omega \left(1 - \frac{\Omega_1(r)}{\Omega} \beta_r \right) \mathbf{e}_\phi \quad (\text{D13})$$

Let us calculate the ratio generally in figure (5) in the equatorial plane

$$\tan(\chi) = \frac{\beta_\phi}{\beta_r} = \frac{\sqrt{g_{rr}g_{\phi\phi}}}{2r} \left[\frac{g_{00}^2}{\beta_r} \frac{d}{dr} \left(\frac{g_{0\phi}}{g_{00}} \right) + \left[\Phi'(r) + \frac{\Omega}{\beta_r} \right] \left(g_{00} \frac{dg_{\phi\phi}}{dr} + g_{0\phi} \frac{dg_{0\phi}}{dr} \right) \right] \quad (\text{D14})$$

Defining a decreasing (dimensionless) function $\delta(r)$ that is the change between the actual shape of the wire and the approximate form (the Archimedean spiral) relative to the latter:

$$\Omega_1(r) = \Omega(1 + \delta(r)) \quad \delta(r) \ll 1 \quad \forall r \gtrsim r_2 \quad \lim_{r \rightarrow \infty} \delta(r) = 0 \quad (\text{D15})$$

At very high energy ($E \rightarrow \infty$),

$$\beta_r \xrightarrow{E \rightarrow \infty} \frac{G_{00}}{G_{0r} + \sqrt{G_{00}G_{rr} + G_{0r}^2}} \quad (\text{D16})$$

Let us get the value of the ratio at the flat light cylinder position $r_{2;flat} = 1/\Omega$ (which is close to the Kerr one, but $r_{2;flat} > r_2$) for the Schwarzschild black hole and expand in small δ

$$\lim_{E \rightarrow \infty} \tan(\chi(r = 1/\Omega))_{a=0} = \frac{1}{2\eta} \left[(1 + \delta)\sqrt{1 - 2\eta} - \sqrt{(1 + \delta)^2 - 2\eta} \right] \approx \frac{-\delta}{\sqrt{1 - 2\eta}} \quad \eta < \frac{1}{2} \quad (\text{D17})$$

In the case of the flat spacetime ($\eta \rightarrow 0$), the ratio does not depend on the rotation at all:

$$\lim_{E \rightarrow \infty} \tan(\chi(r = 1/\Omega))_{M=0} = -\frac{1}{2} \frac{\delta(\delta + 2)}{\delta + 1} \approx -\delta \quad (\text{D18})$$

In the case of a perfect Archimedean spiral, we have a zero ratio exactly in both Schwarzschild and flat spacetimes. Generally speaking, both results are close to zero for small δ . The same analysis can be done in the Kerr case, but we will not include the exact solution. Instead, we show graphically that even in the case of a maximally spinning black hole (which results in a greater value of the azimuthal speed, β_ϕ), the ratio is still close to zero, and can be exactly zero for some variation. For plotting purposes, we consider the following possible values of the variation: $\delta(r = 1/\Omega) \in (0, \frac{1}{2}]$. Moreover, we present these possible values in a form of an exponentially decaying function $e^{-\delta}/2$, where δ here is just a free parameter, not the variation. We choose the allowed values of $\{\eta, a\}$ based on the following constraints:

$$\eta < \frac{1}{a + 2\sqrt{2}} < \frac{1}{2\sqrt{2}} < \frac{1}{2} \quad \eta \sqrt{\frac{(1 - a\eta)}{(1 + a\eta)^3}} < \frac{1}{3\sqrt{3}} \quad (\text{D19})$$

We show in figure (17) that the small variation can cause the ratio in the Kerr case to approach zero at the flat-case light cylinder position. However, this might not be the case for bigger values of η ; in that case, we expect the ratio to approach zero further a bit from the light cylinder (i.e., at some finite $r > 1/\Omega$) because of the decaying nature of the ratio as a function of the radial coordinate r in general.

Moreover, far away from the light cylinder, the ratio in the Kerr case becomes

$$\lim_{E \rightarrow \infty} \tan(\chi(r \gg 1/\Omega)) \approx -\sqrt{\delta(\delta + 2)} + \frac{1 + \delta}{r\Omega} \quad (\text{D20})$$

Thus,

$$\lim_{E \rightarrow \infty} \lim_{r \rightarrow \infty} \tan(\chi) = -\sqrt{\delta(\delta + 2)} \approx -\sqrt{2\delta} \quad (\text{D21})$$

Also, the Lorentz factor (relative to the observer at infinity) far away from the light cylinder for large energy is

$$\gamma_\beta \approx \frac{1 + \delta}{\sqrt{\delta(\delta + 2)}} \approx \frac{1}{\sqrt{2\delta}} \rightarrow \infty \quad (\text{D22})$$

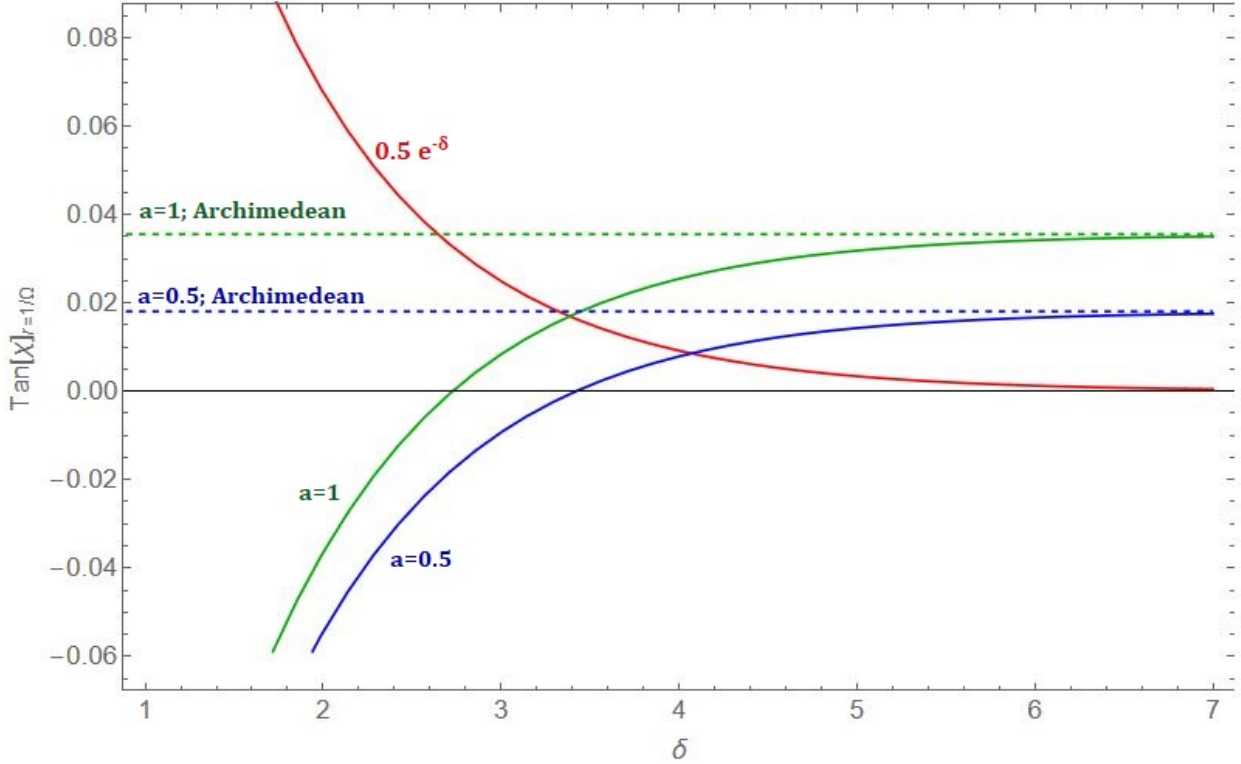


Fig. 17.— The ratio $\tan(\chi) = \beta_\phi/\beta_r$ (for high energy) at the outer light cylinder (in the flat case; i.e., $r = 1/\Omega$) versus a free parameter δ to control the variation in the wire shape from the Archimedean case, for mass-rotation parameter $\eta = 0.1$. The variation allowed range here is $(0, \frac{1}{2}]$, and presented as an exponentially decaying function of the parameter δ , and is plotted in red. We have two sets of curves corresponding to two different wire shapes: the dashed lines correspond to the Archimedean spiral case, and the solid ones correspond to a spiral that is slightly different from the Archimedean one. The colors of the curves correspond to the values of the Kerr parameter: blue curves are for $a = 0.5$ and green curves are for maximally spinning black hole case ($a = 1$). For some variations, the curves meet the horizontal axis, meaning that the ratio is zero.

Next, we calculate the Lorentz factors relative to fixed observers in spacetime and co-rotating observers with the wire. The Lorentz factor can be used to get the speed of the particle as a function of the distance from the black hole singularity. This speed will never exceed the speed of light, unlike the proper speed in (B4), see figure (18). We construct the Lorentz factor in curved spacetimes by imagining filling the (2+1)-D Kerr spacetime with momentarily fixed observers everywhere (only between the ergosphere and the outer light cylinder, as we will show why later). The particle anywhere between the light cylinders is at the same location as exactly one of these observers. At this point, we can obtain a dot product between the four-velocity of the fixed observer and that of the particle, and get an invariant quantity, which is the Lorentz factor of the particle as seen by

the fixed observer where the particle is. The four-velocity of a fixed observer is ($\dot{t} \geq 0, \dot{r} = 0, \dot{\phi} = 0$)

$$U_{fixed}^\mu = \begin{pmatrix} \dot{t} \\ 0 \\ 0 \end{pmatrix} \xrightarrow[\mathcal{L}=-1]{\mathcal{L}=-g_{00}\dot{t}^2} U_{fixed}^\mu = \frac{1}{\sqrt{g_{00}}} \begin{pmatrix} 1 \\ 0 \\ 0 \end{pmatrix} \Rightarrow U_\mu^{fixed} = \left(-\sqrt{g_{00}} \quad 0 \quad \frac{g_{0\phi}}{\sqrt{g_{00}}} \right) \quad (\text{D23})$$

The four-velocity of the particle is

$$U_{particle}^\mu = \begin{pmatrix} \dot{t} \\ \dot{r} \\ \dot{\phi} \end{pmatrix} = \begin{pmatrix} \dot{t} \\ \dot{r} \\ \Phi'(r)\dot{r} + \Omega\dot{t} \end{pmatrix} \quad (\text{D24})$$

The relative Lorentz factor observed by such fixed observers for the particle is

$$\gamma = -U_\mu^{fixed} U_{particle}^\mu = \left(\sqrt{g_{00}} - \frac{\Omega g_{0\phi}}{\sqrt{g_{00}}} \right) \dot{t} - \frac{\Phi'(r)g_{0\phi}}{\sqrt{g_{00}}} \dot{r} \quad (\text{D25})$$

From both (B2) and (B4), the Lorentz factor becomes

$$\gamma = \left(\sqrt{g_{00}} - \frac{\Omega g_{0\phi}}{\sqrt{g_{00}}} \right) \frac{E}{G_{00}} \pm \left(\left(\sqrt{g_{00}} - \frac{\Omega g_{0\phi}}{\sqrt{g_{00}}} \right) \frac{G_{0r}}{G_{00}} - \frac{\Phi'(r)g_{0\phi}}{\sqrt{g_{00}}} \right) \sqrt{\frac{E^2 - G_{00}}{G_{0r}^2 + G_{00} G_{rr}}} \quad (\text{D26})$$

The negative (positive) sign means that the particle is moving towards (away from) the black hole. This Lorentz factor is only defined whenever g_{00} is positive; i.e., outside the ergosphere

$$\mathcal{R} = M \left(1 + \sqrt{1 - a^2 \cos^2 \theta} \right) \quad (\text{D27})$$

See Fig. 18 for a plot of the speed of the particle observed by the fixed observers, which can be obtained from the relation

$$\gamma = \frac{1}{\sqrt{1 - v^2}} \quad (\text{D28})$$

We have a range of allowed values for the constant of motion E . Let r_1 and r_2 be the locations of the light cylinders. From (B4), we get

$$0 < G_{00} \leq E^2, \quad r \in (r_1, r_2) \quad (\text{D29})$$

$$\Omega^2 r^3 - (1 - a^2 \eta^2 - E^2)r + 2M(1 - a\eta)^2 \geq 0 \quad (\text{D30})$$

This is a cubic equation on the form $\Omega^2 r^3 - br + d = 0$ that has to be always non-negative, for all the positive values of r . Therefore, we need to guarantee that the minimum (i.e., extreme) value of the cubic function is also non-negative. We obtain

$$\Omega^2 r^3 - br + d \geq 0, \quad b > 0, d \geq \frac{1}{3\sqrt{3}} \frac{2b^{\frac{3}{2}}}{\Omega} \quad (\text{D31})$$

$$\begin{cases} \sqrt{1 - a^2\eta^2 - 3\eta^{\frac{2}{3}}(1 - a\eta)^{\frac{4}{3}}} \leq E & r \in (r_1, r_2) \\ 0 \leq E < \infty & r > r_2 \end{cases} \quad (\text{D32})$$

The time constant E that appears in (D26) can be related to the initial conditions as observed by a set of fixed observers along the rotating wire. We imagine a set of fixed observers along the rotating wire, only defined between the two light cylinders, and they observe the particle radial speed only. We obtain the relative Lorentz factor as seen by the observers along the wire by applying the same procedure we used to get (D26), but now on the (1+1)-D sub-manifold. The four-velocity of a fixed observer is ($\dot{t} \geq 0, \dot{r} = 0$)

$$U_{fixed}^\mu = \begin{pmatrix} \dot{t} \\ 0 \end{pmatrix} \xrightarrow[\mathcal{L}=-1]{\mathcal{L}=-G_{00}\dot{t}^2} U_{fixed}^\mu = \frac{1}{\sqrt{G_{00}}} \begin{pmatrix} 1 \\ 0 \end{pmatrix} \Rightarrow U_\mu^{fixed} = \left(-\sqrt{G_{00}} \quad \frac{G_{0r}}{\sqrt{G_{00}}} \right) \quad (\text{D33})$$

The four-velocity of the particle is

$$U_{particle}^\mu = \begin{pmatrix} \dot{t} \\ \dot{r} \end{pmatrix} \xrightarrow{(B2)} U_{particle}^\mu = \begin{pmatrix} \frac{G_{0r}\dot{r} + E}{G_{00}} \\ \dot{r} \end{pmatrix} \quad (\text{D34})$$

The radial Lorentz factor of the radially moving particle relative to the fixed observers (on the wire) is the invariant quantity

$$\gamma_r = -U_\mu^{fixed} U_{radial}^\mu = \frac{E}{\sqrt{G_{00}}} = \frac{1}{\sqrt{1 - v_r^2}} \quad (\text{D35})$$

As expected, the radial Lorentz factor coincides with the total one in (D26) in the case of a non-rotating wire:

$$\gamma = \gamma_r = \frac{E}{\sqrt{G_{00}}} = \frac{E}{\sqrt{g_{00}}} \quad (\Omega = 0) \quad (\text{D36})$$

Since the Lorentz factor is always positive, the constant E is always positive too. We can get E easily from the initial conditions as seen by a fixed observer along the wire. If such an observer is at r_0 observes the particle moving along the wire a radial Lorentz factor γ_{r0} , we obtain¹

$$E = \gamma_r \sqrt{G_{00}} = \gamma_{r0} \sqrt{G_{00}(r_0)} \quad (\text{D37})$$

The Lorentz factor in (D26) becomes

$$\begin{aligned} \gamma &= \frac{E}{G_{00}} \left[\left(\sqrt{g_{00}} - \frac{\Omega g_{0\phi}}{\sqrt{g_{00}}} \right) \pm \frac{v_r}{\sqrt{G_{0r}^2 + G_{00} G_{rr}}} \left(\left(\sqrt{g_{00}} - \frac{\Omega g_{0\phi}}{\sqrt{g_{00}}} \right) G_{0r} - \frac{\Phi'(r) g_{0\phi}}{\sqrt{g_{00}}} G_{00} \right) \right] \\ &= \frac{\gamma_r}{\sqrt{G_{00}}} \left[\left(\sqrt{g_{00}} - \frac{\Omega g_{0\phi}}{\sqrt{g_{00}}} \right) \pm \frac{v_r}{\sqrt{G_{0r}^2 + G_{00} G_{rr}}} \left(\left(\sqrt{g_{00}} - \frac{\Omega g_{0\phi}}{\sqrt{g_{00}}} \right) G_{0r} - \frac{\Phi'(r) g_{0\phi}}{\sqrt{g_{00}}} G_{00} \right) \right] \end{aligned} \quad (\text{D38})$$

¹For clarity, the difference between γ_{r0} and γ is that the former is obtained by the observers along (and rotating with) the wire (i.e., in the (1+1)-D sub-manifold); the latter, γ , is obtained by the observers fixed on the Kerr spacetime (i.e., in the (2+1)-D manifold), which contains both the radial and the rotational parts of the speed of the particle.

$$\gamma = \gamma_{r0} \frac{\sqrt{G_{00}(r_0)}}{G_{00}} \left(\sqrt{g_{00}} - \frac{\Omega g_{0\phi}}{\sqrt{g_{00}}} \right) \pm \left(\left(\sqrt{g_{00}} - \frac{\Omega g_{0\phi}}{\sqrt{g_{00}}} \right) \frac{G_{0r}}{G_{00}} - \frac{\Phi'(r)g_{0\phi}}{\sqrt{g_{00}}} \right) \sqrt{\frac{\gamma_{r0}^2 G_{00}(r_0) - G_{00}}{G_{0r}^2 + G_{00} G_{rr}}} \quad (\text{D39})$$

We imagine ejecting the particles on the outer light cylinder ($r = r_2$) with an initial Lorentz factor γ_0 as the initial conditions. Then, we solve for the energy E :

$$\gamma_0 = \lim_{r \rightarrow r_2} \gamma = \frac{1}{2E} \left(\sqrt{g_{00}} - \frac{\Omega g_{0\phi}}{\sqrt{g_{00}}} \right)_{r_2} \left(1 + G_{rr} \left(\frac{E}{G_{0r}} \right)^2 \right)_{r_2} - \left(\frac{\Phi'(r)g_{0\phi}}{\sqrt{g_{00}}} \frac{E}{|G_{0r}|} \right)_{r_2} \quad (\text{D40})$$

$$E = \left\{ \frac{\gamma_0 \pm \sqrt{\gamma_0^2 - \left(\sqrt{g_{00}} - \frac{\Omega g_{0\phi}}{\sqrt{g_{00}}} \right) \left[\left(\sqrt{g_{00}} - \frac{\Omega g_{0\phi}}{\sqrt{g_{00}}} \right) \frac{G_{rr}}{G_{0r}^2} - \frac{2}{|G_{0r}|} \frac{\Phi'(r)g_{0\phi}}{\sqrt{g_{00}}} \right]}}{\left(\sqrt{g_{00}} - \frac{\Omega g_{0\phi}}{\sqrt{g_{00}}} \right) \frac{G_{rr}}{G_{0r}^2} - \frac{2}{|G_{0r}|} \frac{\Phi'(r)g_{0\phi}}{\sqrt{g_{00}}}} \right\}_{r_2} \quad (\text{D41})$$

Therefore, we see that there has to be a minimum initial Lorentz factor for the constant E to have real values. Moreover, we only need the larger energy of the two solutions to guarantee that we have a solution between the light cylinders as well, by being consistent with the constraints (D32). Usually, we have a large Lorentz factor when the particle reaches the outer light cylinder; thus, giving the particle an initial push at the outer light cylinder with a relatively large γ_0 will result in a large amount of the energy:

$$E \approx \gamma_0 \left(\frac{2G_{0r}^2}{\left(\sqrt{g_{00}} - \frac{\Omega g_{0\phi}}{\sqrt{g_{00}}} \right) G_{rr} - 2|G_{0r}| \frac{\Phi'(r)g_{0\phi}}{\sqrt{g_{00}}}} \right)_{r_2} \sim \gamma_0 \quad (\text{D42})$$

For large values of the Lorentz factor of the particle at the outer light cylinder, the energy of the particle behaves the same way as the Lorentz factor of the particle at the outer light cylinder.

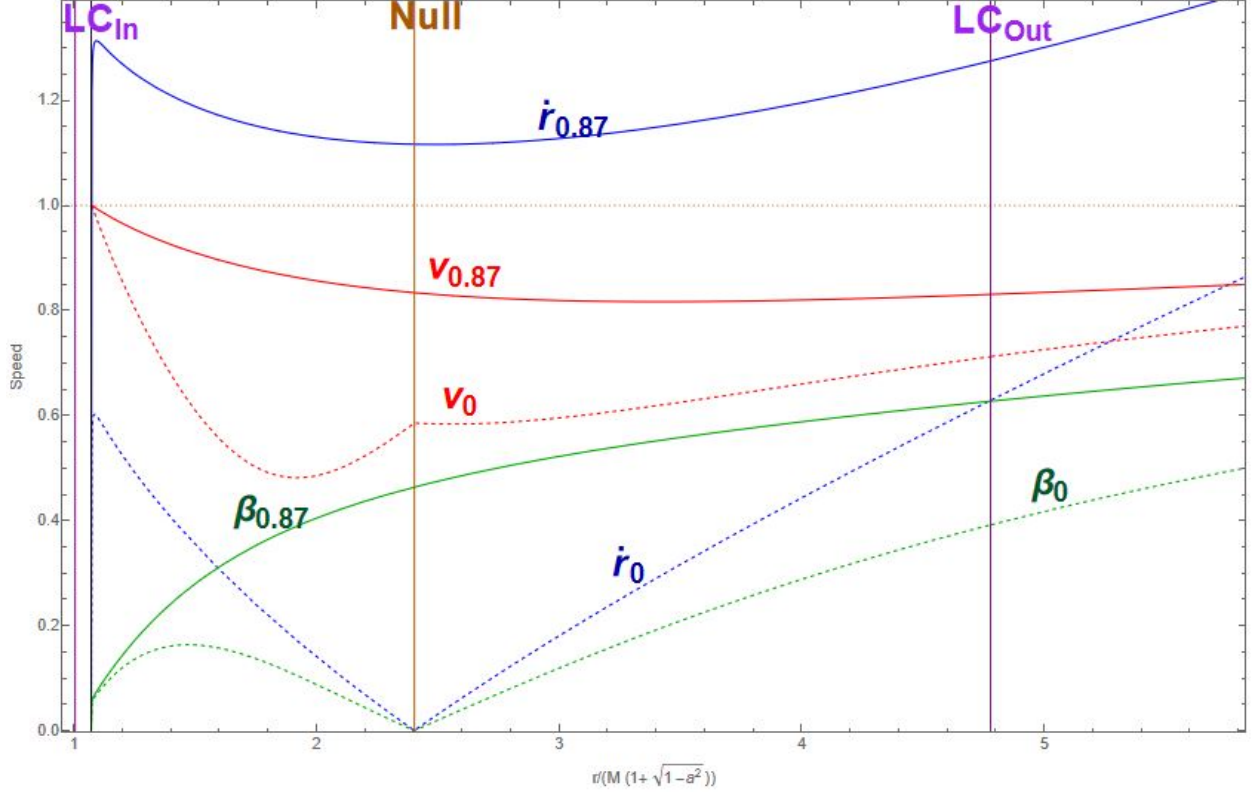


Fig. 18.— Various velocities for a particle moving in Kerr black hole, in the equatorial plane for Kerr parameter $a = 0.5$ and mass-rotation parameter $\eta = 0.1$. The coordinate r here is taken relative to the Kerr horizon $M(1 + \sqrt{1 - a^2})$. We have two sets of curves corresponding to two different initial Lorentz factors γ_{r0} in (D35) at the null line: the dashed curves correspond to a zero initial speed ($\gamma_{r0} = 1$), and the solid ones correspond to an initial speed of 0.87 of the speed of light ($\gamma_{r0} \approx 2.03$). The colors of the curves correspond to the different kinds of speeds: (i) blue curves are the proper speed, \dot{r} in (B4); (ii) green curves are speed β_r , the speed measured by an observer at infinity (iii) red curves are the speed correspond to the Lorentz factor in (D39). The dotted (brown) horizontal line at 1 is plotted to indicate the speed of light (we see that $dr/d\tau$ exceeds the speed of light between the two light cylinders, while the other two speeds do not). The vertical lines are colored as follows: purple for both light cylinders (the inner one is so close to the Kerr horizon at 1); brown for the null line, which lies between the light cylinders; and, black for the ergosphere (D27). The ergosphere lies before the null line due to a condition on both η , a , in addition to the condition (D4): $|a - \eta^{-1}| > 2\sqrt{2}$. Finally, we only plotted the speeds outside the ergosphere ($\mathcal{R} = 2M$ here) because the Lorentz factor in (D39) is only defined after such radius.